

Suzaku broad band observations of the Seyfert 1 galaxies Mrk 509 and Mrk 841

M. Cerruti¹, G. Ponti², C. Boisson¹, E. Costantini³, A.L. Longinotti⁴, G. Matt⁵, M. Mouchet^{6,1}, and P.O. Petrucci⁷

¹ LUTH, Observatoire de Paris, CNRS, Université Paris Diderot; 5 Place Jules Janssen, 92190 Meudon, France
e-mail: matteo.cerruti@obspm.fr

² School of Physics and Astronomy, University of Southampton, Highfield, Southampton SO17 1BJ, UK

³ SRON, Netherlands Institute for Space Research, Sorbonnelaan 2, 3584 CA Utrecht, The Netherlands

⁴ MIT, Kavli Institute for Astrophysics and Space Research, 77 Massachusetts Avenue, NE80-6011, Cambridge, MA, 02139, U.S.A.

⁵ Dipartimento di Fisica, Università degli Studi Roma Tre, Via della Vasca Navale 84, 00146 Roma, Italy

⁶ APC, Université de Paris 7 Denis Diderot, 75205 Paris Cedex, France

⁷ UJF-Grenoble 1 / CNRS-INSU, Institut de Planétologie et d'Astrophysique de Grenoble (IPAG) UMR 5274, Grenoble, F-38041, France

Received 6 January 2011/ Accepted 22 August 2011

Abstract

Context. Markarian 509 and Markarian 841 are two bright Seyfert 1 galaxies with X-ray spectra characterised by a strong soft excess and a variable Fe $K\alpha$ line, as shown by several X-ray observatories in the past.

Aims. In this paper we report an analysis and modelling of new *Suzaku* observations of these sources, taken between April and November, 2006, for Mrk 509, and January and July, 2007, for Mrk 841, for a total exposure time of ≈ 100 kiloseconds each. Data from *XIS* and *HXD/PIN* instruments, going from 0.5 to 60 keV, represent the best resolution simultaneous broad band X-ray spectrum for these objects, and should bring more constraints on the origin of the soft excess emission.

Methods. We fitted the broad band spectrum of both sources with a double Comptonisation model, adding a neutral reflection from distant material and a two-phase warm absorber. We then studied the two competitive models aimed to explain the soft excess with atomic processes: a blurred ionised disc reflection and an ionised absorption by a high velocity material.

Results. When fitting the data in the 3–10 keV range with a power law spectrum, and extrapolating this result to low energies, a soft excess is clearly observed below 2 keV: its strength is however weak compared to past observations of both sources. A moderate hard excess is seen at energies greater than 10 keV, together with a neutral Fe $K\alpha$ narrow emission line at $E_0 \approx 6.4$ keV and a broad Fe emission line. For Mrk 509, the broad Fe emission line is required in all the three physical models in order to have a good fit to the data: this finding suggests that the blurred reflection model correctly describes the soft excess, but it underestimates the broad Fe emission line; on the other hand, for the smeared absorption model, this suggests that the continuum spectrum absorbed by the outflowing gas should contain indeed a reflected component. For Mrk 841, the three models we tested give a good fit to the data, and we cannot invalidate any of them; a broad emission line is required in the double Comptonisation and smeared absorption models, while the blurred reflection model consistently fits the broad band spectrum, without adding any extra-emission line component.

Key words. galaxies: Seyfert – galaxies: individuals: Mrk509, Mrk841, PKS1502+106 – X-rays: galaxies

1. Introduction

The origin of the soft X-ray excess emission is still nowadays, about three decades after the discovery (Pravdo et al. 1981; Arnaud et al. 1985), one of the major open questions in AGN (Active Galactic Nuclei) research (e.g. Turner & Miller 2009). This component appears like a featureless excess of emission above the low energy extrapolation of the 2–10 keV best fit power law. Historically associated with the high energy tail of the accretion disc black body radiation, many authors (Czerny et al. 2003; Gierliński & Done 2004, hereafter GD04; Piconcelli et al. 2005; Crummy et al. 2006, hereafter C06) have shown that a modelling with a thermal continuum implies a characteristic “temperature” higher than expectations (Shakura & Sunyaev 1976) and that remains remarkably constant across a range of AGN despite a wide spread in black hole mass and AGN luminosity. Moreover, in bright and variable AGN the soft excess does not follow the expected black body luminosity-temperature relation (Ponti et al. 2006). Samples of AGN show that the ratio of the soft excess, at 0.5 keV, above the extrapolation of the high

energy power law emission has a very small scatter (Piconcelli et al. 2005; Miniutti et al. 2009), very different from what is observed in galactic black holes in the bright soft state, dominated by the disc black body emission (e.g. Done et al. 2007). These findings triggered the search for a different origin for the soft excess. The first idea investigated has been Comptonisation that may occur in the upper layer of the accretion disc (Czerny et al. 2003; GD04; Sobolewska & Done 2007). This model may explain the featureless shape of the soft excess and its high temperature; the feedback between coronal disc irradiation and the disc skin may provide a mechanism to stabilize the soft excess temperature and emission ratio compared to the power law emission. On the other hand, the observed constancy of the soft excess temperature seems to suggest a nature tied to atomic processes. Two possible alternatives are reflection and absorption. If the upper layer of the accretion disc is ionized the disc Compton reflection component will contain many X-ray lines (Ross & Fabian 2005) that will be broadened by the relativistic motion of the material on the surface of the accretion

Table 1. *Suzaku* observations log.

Mrk 509				
	ID	Aim Point	Start	Exposure (s)
obs.1	701093010	HXD	2006-04-25	24580
obs.2	701093020	XIS	2006-10-14	25960
obs.3	701093030	XIS	2006-11-15	24450
obs.4	701093040	XIS	2006-11-27	33090
tot				108080
Mrk 841				
	ID	Aim Point	Start	Exposure (s)
obs.1	701084010	HXD	2007-01-22	51790
obs.2	701084020	HXD	2007-07-23	50930
tot				102720

disc, forming a featureless continuum (C06). On the other hand, ionized absorption processes imprint their main features in the soft X-ray band. If these absorbers are relativistically moving (for example, in the form of a disc wind) they may, as well, produce a featureless curved continuum and reproduce the soft excess. Nevertheless, numerical simulations indicate that, in order to reproduce the excess, the velocities of such a wind have to be extremely high (Schurch & Done 2008), suggesting that the flow has to be clumpy and/or only partially covering the source, or associated with a magnetically driven jet.

These different models are degenerate in the 0.5-10 keV band but still predict different amounts of hard X-ray emission. In addition these models produce different variability behaviour in the soft and hard energy band and, thus, the measurement of the high energy flux may help to disentangle them. With this aim, we observed with *Suzaku* Markarian 509 (Mrk 509), the brightest Seyfert 1 galaxy in the hard X-ray sky (17-60 keV), with an important soft excess and without a strong warm absorber component (Sazonov et al. 2007), and Markarian 841 (Mrk 841), one of the first AGN in which a soft excess has been discovered (Arnaud et al. 1985). Informations about the four Mrk 509 observations and the two observations of Mrk 841 are given in Table 1.

Mrk 509, located at a redshift of $z = 0.0344$ (Fisher et al. 1995), was first observed at X-rays energies by *Ariel V* (Cooke et al. 1978), and then studied by several X-rays telescopes. *HEAO-1* (Singh et al. 1985) detected its soft excess for the first time; this feature was later confirmed by *EXOSAT* (Morini et al. 1987), together with the detection of a Fe $K\alpha$ emission line; *Ginga* (Singh et al. 1990) revealed a hardening of the power law at energies greater than 10 keV; later on, *BeppoSAX* observations (Perola et al. 2000) suggested a power law cut-off at 70 keV and revealed informations about the warm absorber (Dadina et al. 2005), which has been deeply studied by Smith et al. (2007) and Detmers et al. (2010), with *XMM-Newton/RGS* data; Ponti et al. (2009) presented the most complete study of Fe K complex, using *XMM-Newton* data and the same *Suzaku* observations we present here: for this reason, in this paper we will focus on broad band spectrum only, and no further analysis of emission lines will be done. Recently, a multi-wavelength campaign on this source has been carried on, using data from seven different satellites and observatories (from infra-red to hard X-rays): see Kaastra et al. (2011) and references therein.

Mrk 841 ($z = 0.0365$) is a bright Seyfert 1 galaxy, and its soft excess was first detected by *EXOSAT* (Arnaud et al. 1985). As for Mrk 509, Mrk 841 is a deeply studied source.

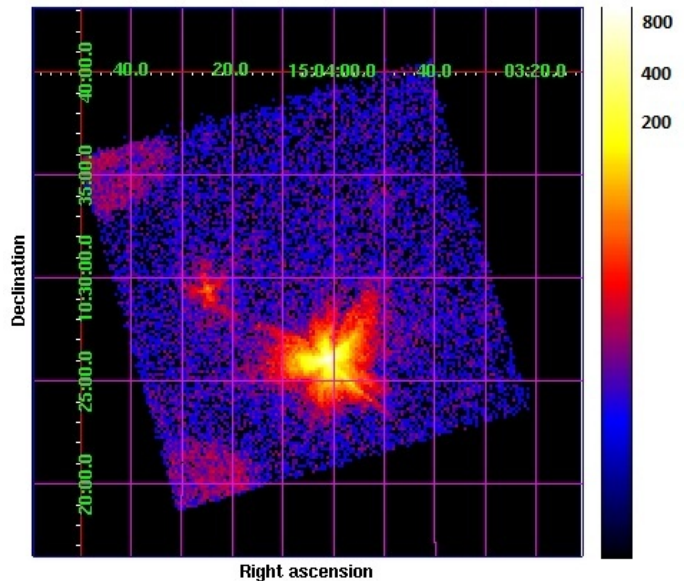


Figure 1. *Suzaku/XIS0* image of Mrk 841 (first observation): the brightest source is Mrk 841 and the fainter one is consistent with PKS 1502+106; the two calibration spots are visible in the top and bottom left corners.

George et al. (1993) gave first evidence of Fe $K\alpha$ emission line detection and broad band variability; in a 24 type 1 AGN sample observed by *ASCA* (Reynolds 1997), Mrk 841 belongs to sources for which a "statistically significant soft excess" is observed; more recent observations have been performed by *BeppoSAX* (Bianchi et al. 2001) and *XMM-Newton* (Petrucci et al. 2007, hereafter P07; Longinotti et al. 2010). P07 studied in detail Fe K complex variability, while Longinotti et al., with *XMM-Newton/RGS* data, investigated the warm absorber structure. Even though the goal of this paper is to investigate the broad band X-ray spectrum of this object, in Section 3.4 we will also discuss the Fe $K\alpha$ narrow emission line detection.

The paper is organised as follow: in Section 2 we detail the *Suzaku* data reduction and we present the serendipitous detection of the blazar PKS 1502+106; in Section 3.1 we study the light curves of Mrk 509 and Mrk 841; in Section 3.2 we analyse the soft X-ray excess in both sources and in Section 3.3 we discuss their hard excess; in Section 3.4 we concentrate on the Fe $K\alpha$ narrow emission line detection in Mrk 841; Section 3.5 is dedicated to the modelling of the broad band (*XIS* and *PIN*) *Suzaku* summed spectra in a double Comptonisation scenario, discussing the detection of a warm absorber in both sources; in Sections 3.6 and 3.7 we fit the broad band summed spectra with a blurred ionised reflection model and a smeared ionised absorption one. The discussion and the conclusions are in Section 4.

2. Data Reduction

Suzaku X-ray telescope carries two main instruments: *XIS* (Koyama et al. 2007), a soft (0.2-12 keV) X-ray Imaging Spectrometer, and *HXD* (Takahashi et al. 2007), a Hard X-ray Detector which covers the higher energy domain (10-500 keV).

XIS is composed of four CCD cameras: three of them (*XIS0,2,3*) are front-illuminated (*FI*), while one (*XIS1*) is back-illuminated (*BI*). Due to a failure, *XIS2* is unavailable for observations performed after November 9, 2006: for uniformity between observations, we did not consider data from this instrument.

Event files from version 2.0.6.13 of the *Suzaku* pipeline processing were used, with standard screening criteria, and data were then reduced using version 6.7 of *HEASoft*¹. Spectra and light curves were extracted using *XSelect*, version 2.4a. The chosen extracting region is large enough ($r > 150$ arcsec) to avoid calibration problems (as suggested in the *Suzaku* ABC Guide²). The background has been extracted from a region (circular or annular, according to the aim point) in the same image, respecting the same geometrical constraints as for the source. Response matrices and ancillary response files were generated for each *XIS* using *xismfgen*, version 2009-02-28, and *xissimarfgen*, version 2009-01-08, tools. The two *XIS/FI* spectra have been added using *mathpha* with 'POISS-3' error propagation method, which represents a mean value between the two extreme error values 'POISS-1' and 'POISS-2' (see *mathpha* user's guide³ and references therein). Response files have been added using *addrmf*, version 1.21, and *addarf*, version 1.2.6. A single *XIS* lightcurve has been obtained summing up the three *XIS0,1* and 3 background subtracted lightcurves, using *XRonos*, version 5.22.

HXD is composed of two detectors: *PIN* (Positive Intrinsic Negative diodes; 10-60 keV) and *GSO/BGO* (Gadolinium Silicate/Bismuth Germanate crystals; 50-500 keV). In this paper we present data from *PIN* only, since no significant signal was detected from *GSO*. For *HXD/PIN*, Non-X-ray Instrumental Background (NXB) and response matrices provided by the *HXD* instrument team have been used. An additional component for the CXB (Cosmic X-ray Background) (Boldt & Leiter 1987) has been included and added to the NXB using *mathpha*, version 4.1.0. Spectra have been corrected for the dead time, using *hxdtdcor*, version 1.50, and background exposure time has been increased by a factor ten, following the *Suzaku* ABC Guide. For Mrk 841 observations, PKS 1502+106 (see section 2.1) is in the *PIN* field of view, and its flux, as extrapolated from *XIS* observations, has been added with *mathpha* to the background.

Each spectrum has been rebinned according to the following procedure: for *XIS*, we checked the true energy resolution of each instrument, extracting the spectrum of the calibration spots in CCD camera (see Fig. 1), and measuring the energy and the FWHM (Full Width at Half Maximum) of the Mn $K\alpha$ line; with these values, and using equation (1) given in Koyama et al. (2007), we get the true *XIS* energy resolution as a function of energy; for *PIN*, we used energy resolution values given in Takahashi et al. (2007); then we rebinned the data in order to have 5 bins for each energy resolution element. In order to use a χ^2 minimization algorithm, we imposed a minimum number of counts per bin: this second rebinning does affect the first and the last bins of the spectra only, while in the other channels the condition of 5 bins per resolution element is always dominant. We chose a minimum of 30 (for Mrk 841) and 50 (for Mrk 509) counts per bin, leading to a similar number of bins for both

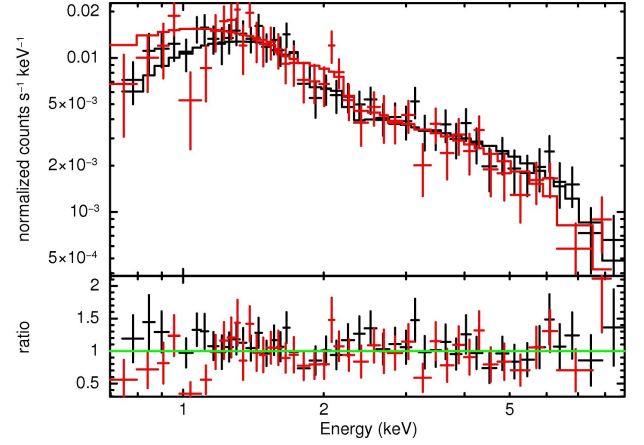


Figure 2. PKS 1502+106 spectrum (observer frame) as seen by *Suzaku/XIS/FI* (black) and *XIS1* (red). Data have been fitted with a power law model absorbed by galactic material (see section 2.1): data-to-model ratio is shown in the bottom plot.

sources. We considered *XIS/FI* data in the energy band 0.6-10 keV, and *XIS1* data in the range 0.5-8.5 keV; *XIS* data comprised between 1.62 and 1.82 keV have been ignored (due to a known calibration problem around the Si K edge⁴); *PIN* data below 15 keV have been ignored, and the last *PIN* significant bin is at ≈ 33 keV for Mrk 841 and ≈ 38 keV for Mrk 509.

We also studied the summed spectra of the sources, adding *XIS* and *PIN* data from different observations. For Mrk 509, the first observation has not been included in the summed spectrum, because it has been performed with an aim point different than the others. Source and background spectral files from different observations have been added using the same procedure described above for the sum of *XIS/FI* spectra. In order to take into account the relative normalization between different instruments during the fitting, models for each instrument data have been multiplied by a constant, as indicated by Maeda et al. (2008)⁵. Spectral fitting has been performed with *XSpec*, version 12.5.1. Parameter errors in text and tables are given at 90% confidence level. We assume a flat cosmology with $H_0 = 70 \text{ km s}^{-1} \text{ Mpc}^{-1}$ and $\Omega_\Lambda = 0.73$.

2.1. Contaminating Source: PKS 1502+106

Figure 1 shows the *Suzaku/XIS0* image of the first observation of Mrk 841. The brightest source at the *HXD* aim point position is Mrk 841, while a second bright source appears in the field of view (at a distance of about $7'$ from Mrk 841), coincident with PKS 1502+106. This source, situated at $z = 1.839$ (Smith et al. 1977), has been recently classified as a blazar (Abdo et al. 2010). We extracted the spectrum of this source following the same procedure discussed in the previous section: Fig. 2 shows the *XIS* spectrum of PKS 1502+106. We fitted the spectrum with a simple power law absorbed by galactic material (model *wabs*powerlaw* in *Xspec*, with $N_H = 2.36 \cdot 10^{20} \text{ cm}^{-2}$, Dickey & Lockman (1990)). The best fit photon index is

¹ <http://heasarc.nasa.gov/lheasoft>

² <http://heasarc.gsfc.nasa.gov/docs/suzaku/analysis/abc/>

³ http://heasarc.gsfc.nasa.gov/docs/heasarc/caldb/docs/memos/ogip_95_008/ogip_95_008.pdf

⁴ <http://heasarc.nasa.gov/docs/suzaku/analysis/sical.html>

⁵ <http://www.astro.isas.ac.jp/suzaku/doc/suzakumemo/suzakumemo-2008-06.pdf>

$\Gamma = 1.32 \pm 0.08$ ($\chi^2 = \chi^2 / (\text{Degrees Of Freedom (DOF)}) = 71/86$). The source flux in the 0.5-2 keV and 2-10 keV bands is $2.2^{+0.3}_{-0.3}$ and $7.5^{+0.6}_{-0.7} \cdot 10^{-13} \text{ ergs cm}^{-2} \text{ s}^{-1}$ respectively. The 2-10 keV luminosity is $1.8^{+0.2}_{-0.1} \cdot 10^{46} \text{ ergs s}^{-1}$. PKS 1502+106 has been widely observed in the past, showing a photon index Γ varying between 1.4 and 1.9 and a 2-10 keV flux in the range $4.9 - 6.54 \cdot 10^{-13} \text{ ergs cm}^{-2} \text{ s}^{-1}$ (George et al. 1994; Akiyama et al. 2003; Watanabe et al. 2004). Recently an outburst has been observed by Fermi and Swift (Abdo et al. 2010), with $F_{0.3-10 \text{ keV}} = 2.18 \cdot 10^{-12} \text{ ergs cm}^{-2} \text{ s}^{-1}$, and $\Gamma = 1.54$. *Suzaku* observation suggests that PKS 1502+106 has been detected during quite a high state, but not during an outburst (light curve does not show any significant variability). However, the power law index is consistent with a low state of the source. This source falls within the *PIN* field of view, thus it has a contribution in the *PIN* data. The extrapolated flux in the 12-60 keV band is $2.5 \cdot 10^{-12} \text{ ergs cm}^{-2} \text{ s}^{-1}$. This component has been included in the *PIN* background.

During the second observation, PKS 1502+106 falls off the CCD image of Mrk 841, but it is still present in the *PIN* field of view: we subtracted from *PIN* data the same spectrum evaluated for the first observation.

No bright X-ray sources are observed in the *XIS* field of view of Mrk 509.

3. Data analysis

3.1. Light Curves

XIS light curves of Mrk 509 and Mrk 841 are shown in Fig. 3. Due to *Suzaku* orbit, the targets, periodically occulted by Earth, cannot be observed continuously and light curves are composed by several blocks of a few kiloseconds each. As no significant variability appears at this time scale, we decided to rebin the data to one bin per observation window. Light curves have been extracted in two energy bands, a soft (0.5-3 keV) one and a hard (3-10 keV) one, and a count-rate hardness ratio ($h = \text{hard}/\text{soft}$) has been evaluated. *PIN* light curves are always compatible with a constant flux.

During the first observation of Mrk 509, the source was in the *HXD* aim point, which provides a lower ($\approx 10\%$) effective area and a lower number of counts per second than for the *XIS* aim point (which has been used for the three other observations). For this reason, the lightcurve of obs.1 has to be corrected for this systematic error when compared to the other observations. Taking into account this effect, Mrk 509 presents a variability of $\approx 25\%$ between the four observations in the soft energy band, but within a single observation the flux variation is only 11-14%, reaching 20% only during the last observation. In the hard energy domain, the variability is $\approx 16\%$ between observations and $\approx 15\%$ (but 20% during the fourth observation) on 10^5 s timescale.

The value of the hardness ratio during obs. 1, 2 and 4 is compatible with a constant (the mean values are $h = 0.27^{+0.01}_{-0.01}$, $0.26^{+0.01}_{-0.01}$ and $0.27^{+0.01}_{-0.01}$, respectively). During the third observation h has instead a lower value ($0.24^{+0.01}_{-0.01}$). Miyazawa et al. (2009) analysed the temporal and spectral variability of a sample of 36 AGN observed by *Suzaku*: the four observations of Mrk 509 we present here, are part of this sample, and a correlation plot between the 0.5-2 keV and the 2-10 keV light curves is shown (see Fig.3 in their paper). They found a correlation between the fluxes in the soft and the hard energy

band, consistent with the nearly constancy of the hardness ratio, though the lower value of h during the third observation increases the dispersion in the correlation plot.

The two Mrk 841 observations have an almost equal mean flux value, but the source shows variability on time scale of 10^5 s (26 and 46% in the soft X-ray domain, and 32 and 42% in the hard X-ray domain, for the two observations respectively). For this source, too, the hardness ratio is nearly constant, and we measure a mean value of $h = 0.29^{+0.02}_{-0.02}$.

Given the low variability observed in Mrk 509 and Mrk 841 light curves, and in order to improve the signal-to-noise ratio, in the following we study the summed spectra as well as individual observations for phenomenological models.

3.2. Soft Excess

We start the analysis considering the *XIS* 3-10 keV energy band. We model the data using a power law plus two narrow gaussian functions (model *zgauss* in *XSpec*, assuming $\sigma = 0$) for the Fe $K\alpha$ and $K\beta$ narrow emission lines (assuming $E_{K\beta} = 7.06$ keV and imposing its normalization factor $C_{K\beta}$ equal to $0.15 C_{K\alpha}$ (Palmeri et al. 2003)). An excess of emission is clearly observed around 6.4 keV (see Fig. 4) and adding a broad emission line significantly improves the fit (F-test probability equal to $4 \cdot 10^{-21}$ and $7 \cdot 10^{-7}$ for the summed Mrk 509 and Mrk 841 data set, respectively). Table 2 shows the best fit results. The detection of a Fe broad emission line in *Suzaku* observations is consistent with the results showed in the FEROS (Finding Extreme Relativistic Objects) survey (de La Calle Pérez et al. 2010), which studied, using *XMM-Newton* data, the relativistic Fe $K\alpha$ emission lines in Seyfert 1 galaxies, including Mrk 509.

Ponti et al. (2009) studied in detail the Fe K complex in Mrk 509, using the same *Suzaku* observations presented here: in particular, they showed that a broad Fe line (with parameters consistent with our values given in Table 2) represents the best-fitting model, compared to a possible blend of narrow Fe lines.

For Mrk 841, we tested as well the possibility that a blending of H-like and He-like lines of Fe can be responsible of the broad line observed: however, this model (two narrow gaussian lines, with energies fixed to 6.67 and 6.97 keV, plus the 6.4 and 7.06 Fe lines, as described above), does not improve significantly the goodness of the fit (F-test probability equal to 0.1 for the summed data-set).

Mrk 509 shows variability in the 3-10 keV flux (it is comprised between 3.39 and $3.78 \cdot 10^{-11} \text{ ergs cm}^{-2} \text{ s}^{-1}$), while the slope is consistent, within errors, with a constant (the two extreme values are $1.79^{+0.04}_{-0.03}$ and $1.86^{+0.05}_{-0.04}$ for the second and the third observation, respectively); Mrk 841 observations are quite similar ($\Gamma = 1.75$ - 1.77 and $F = 1.10$ - $1.11 \cdot 10^{-11} \text{ ergs cm}^{-2} \text{ s}^{-1}$), as discussed in the previous section.

It is useful to compare these results to past observations. *BeppoSAX* (De Rosa et al. 2004) detected Mrk 509 in two quite different states, at $F_{2-10 \text{ keV}} = 2.7$ and $5.7 \cdot 10^{-11} \text{ ergs cm}^{-2} \text{ s}^{-1}$ with $\Gamma = 1.80$ - 1.59 respectively (for comparison Mrk 509 2-10 keV flux during the four *Suzaku* observations varies between 4.3 and $4.8 \cdot 10^{-11} \text{ ergs cm}^{-2} \text{ s}^{-1}$, setting these observations in an intermediate state); *XMM-Newton* (Smith et al. 2007) observed the source in a even lower state at $F_{0.5-10 \text{ keV}} = 2.6 \cdot 10^{-11} \text{ ergs cm}^{-2} \text{ s}^{-1}$.

Mrk 841 has been observed by *XMM-Newton* (see P07) at $F_{3-10 \text{ keV}} = 0.8$ - $1.3 \cdot 10^{-11} \text{ ergs cm}^{-2} \text{ s}^{-1}$ with $\Gamma = 1.30$ -

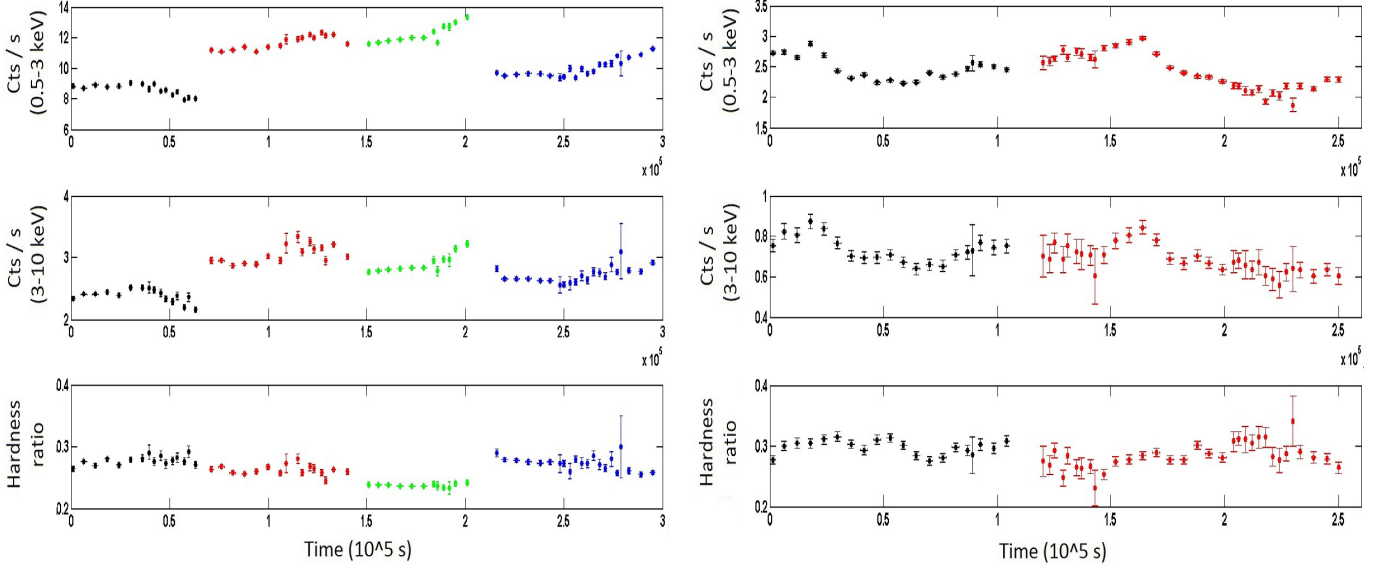


Figure 3. Mrk 509 (left) and Mrk 841 (right) light curves. Different observations are shown in different colours (one-black, two-red, three-green and four-blue). From top to bottom: 0.5-3 keV light curve (in units of counts per second); 3-10 keV light curve and hardness ratio (3-10/0.5-3). Gap between observations is arbitrary.

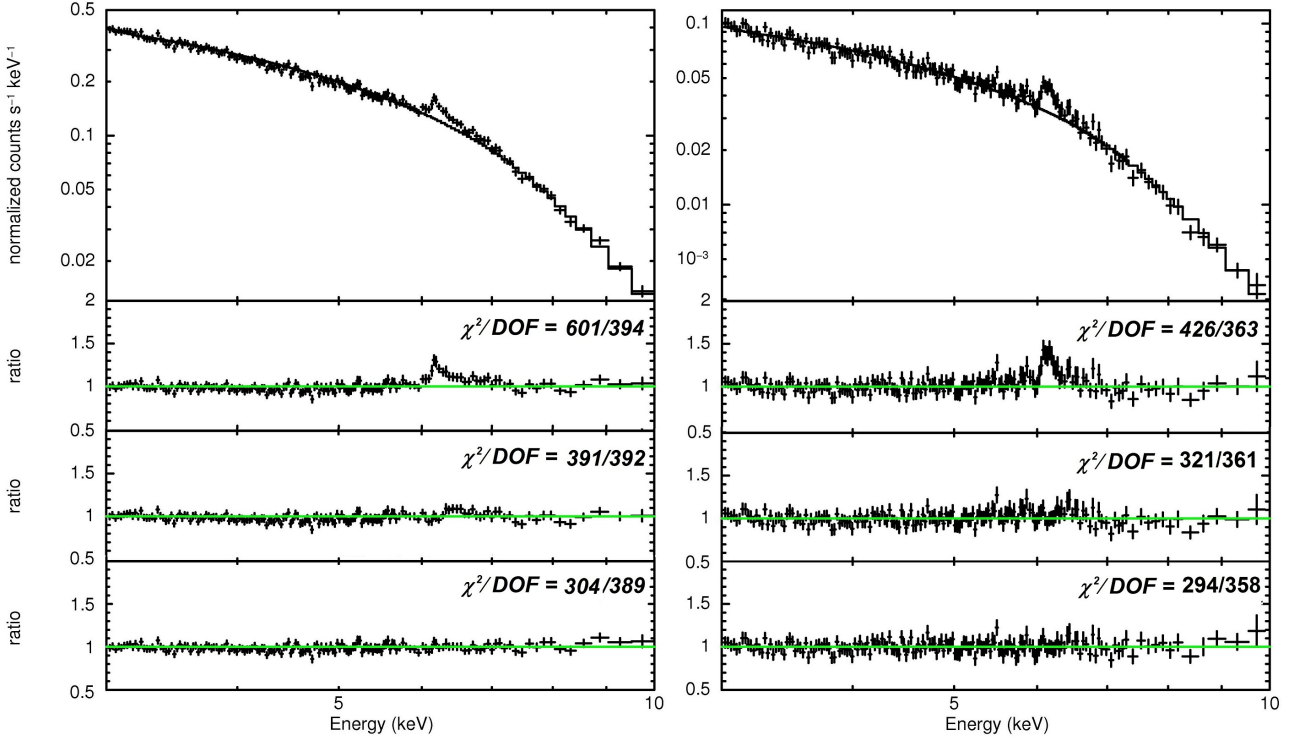


Figure 4. XIS data between 3 and 10 keV of the sum of Mrk 509 (left) and Mrk 841 (right) observations : data are first fitted with a power law (ignoring the 6-7 keV energy band, upper panel and first ratio plot); then two narrow gaussian lines (for the Fe $K\alpha$ and $K\beta$ emission lines, see section 3.2) are added to the fit (second ratio plot); a broad ($\sigma > 0$) Fe emission line is finally considered (third and last ratio plot). Only FI data are shown, as they have the best resolution around the Fe $K\alpha$ emission line, but the fit has been performed using both FI and XIS1 data. The energy on the abscissa is in the observer frame. The data have been rebinned for clarity purposes.

1.95. Compared to these values, the source was in an intermediate state during *Suzaku* observations; in the past Mrk 841 has been seen in a quite low state by Pounds et al. (1994) (simultaneous *Ginga* and *ROSAT* observations) with

$$F_{2-10 \text{ keV}} = 7.9 \cdot 10^{-12} \text{ ergs cm}^{-2} \text{ s}^{-1}.$$

Extrapolating the power law fit between 3 and 10 keV to low energies, an excess of photons is observed: in Fig. 5 we report XIS1 spectra for Mrk 509 and Mrk 841, and for each

Table 2. Best fit parameter values for the model $powerlaw + zgauss + zgauss + zgauss$, considering *XIS* data between 3 and 10 keV. The three gaussian functions model the Fe $K\alpha$ and $K\beta$ narrow emission lines (with $\sigma = 0$) and the broad Fe K emission line. Fe $K\beta$ emission line has been frozen in energy ($E_{K\beta} = 7.06$ keV) and in normalization (imposed equal to 0.15 times the $K\alpha$ line normalization). Γ is the power law photon index; the power law normalization C_Γ is the number of photons $\text{keV}^{-1} \text{cm}^{-2} \text{s}^{-1}$ at 1 keV; the line normalization parameters $C_{K\alpha}$ and C_{br} are the integrated number of photons $\text{cm}^{-2} \text{s}^{-1}$ in the line; σ_{br} is the line width expressed in keV; EqW is the line equivalent width expressed in eV; the flux F , evaluated between 3 and 10 keV, is given in units of $\text{ergs cm}^{-2} \text{s}^{-1}$. For the summed spectra, the results of a *XIS* (above 3 keV) + *PIN* fit are reported as well (last line): the R_{pexrav} parameter represents the *pexrav* reflection scaling factor (see Section 3.3).

Mrk 509												
Obs.	Γ	C_Γ (10^{-3})	$E_{K\alpha}$ (keV)	$C_{K\alpha}$ (10^{-5})	$EqW_{K\alpha}$ (eV)	E_{br} (keV)	C_{br} (10^{-5})	σ_{br} (keV)	EqW_{br} (eV)	R_{pexrav}	F (10^{-11})	χ^2/DOF
1	$1.80^{+0.05}_{-0.04}$	$12.5^{+0.8}_{-0.6}$	$6.42^{+0.09}_{-0.09}$	$0.9^{+0.9}_{-0.8}$	16^{+18}_{-15}	$6.44^{+0.17}_{-0.16}$	$6.2^{+3.6}_{-2.7}$	$0.44^{+0.28}_{-0.17}$	126^{+79}_{-78}		$3.45^{+0.02}_{-0.03}$	329/386
2	$1.79^{+0.04}_{-0.03}$	$13.4^{+0.2}_{-0.3}$	$6.47^{+0.06}_{-0.06}$	$1.6^{+0.8}_{-0.7}$	28^{+19}_{-18}	$6.51^{+0.17}_{-0.18}$	$4.6^{+3.0}_{-2.2}$	$0.41^{+0.30}_{-0.18}$	86^{+50}_{-61}		$3.78^{+0.02}_{-0.02}$	375/366
3	$1.86^{+0.05}_{-0.04}$	$14.4^{+0.4}_{-0.7}$	$6.41^{+0.05}_{-0.05}$	$1.7^{+0.9}_{-0.8}$	30^{+19}_{-17}	$6.55^{+0.25}_{-0.14}$	$5.7^{+1.8}_{-1.8}$	$0.44^{+0.29}_{-0.14}$	112^{+43}_{-45}		$3.60^{+0.03}_{-0.02}$	344/352
4	$1.80^{+0.04}_{-0.03}$	$12.1^{+0.7}_{-0.6}$	$6.42^{+0.03}_{-0.03}$	$1.8^{+0.7}_{-0.7}$	35^{+15}_{-15}	$6.71^{+0.21}_{-0.14}$	$6.7^{+3.2}_{-2.4}$	$0.52^{+0.25}_{-0.20}$	145^{+75}_{-65}		$3.39^{+0.02}_{-0.02}$	396/378
2+3+4	$1.84^{+0.03}_{-0.02}$	$13.5^{+0.5}_{-0.4}$	$6.43^{+0.03}_{-0.03}$	$1.7^{+0.4}_{-0.5}$	31^{+6}_{-6}	$6.63^{+0.11}_{-0.09}$	$6.6^{+2.2}_{-1.7}$	$0.50^{+0.17}_{-0.12}$	135^{+48}_{-45}		$3.50^{+0.01}_{-0.02}$	304/389
+PIN	$1.88^{+0.05}_{-0.05}$	$14.0^{+0.6}_{-0.8}$	$6.43^{+0.03}_{-0.03}$	$1.7^{+0.5}_{-0.5}$	33^{+9}_{-14}	$6.69^{+0.16}_{-0.13}$	$6.1^{+3.8}_{-1.4}$	$0.56^{+0.34}_{-0.17}$	126^{+29}_{-67}	$0.4^{+0.2}_{-0.2}$	$3.50^{+0.02}_{-0.02}$	319/405
Mrk 841												
Obs.	Γ	C_Γ (10^{-3})	$E_{K\alpha}$ (keV)	$C_{K\alpha}$ (10^{-5})	$EqW_{K\alpha}$ (eV)	E_{br} (keV)	C_{br} (10^{-5})	σ_{br} (keV)	EqW_{br} (eV)	R_{pexrav}	F (10^{-11})	χ^2/DOF
1	$1.77^{+0.08}_{-0.05}$	$3.77^{+0.20}_{-0.19}$	$6.39^{+0.02}_{-0.03}$	$1.0^{+0.3}_{-0.3}$	58^{+26}_{-22}	$6.03^{+0.36}_{-0.31}$	$2.7^{+2.7}_{-0.9}$	$0.74^{+0.32}_{-0.31}$	156^{+105}_{-119}		$1.10^{+0.03}_{-0.03}$	303/341
2	$1.75^{+0.06}_{-0.05}$	$3.66^{+0.10}_{-0.25}$	$6.38^{+0.04}_{-0.04}$	$0.7^{+0.3}_{-0.4}$	39^{+32}_{-26}	$6.26^{+0.18}_{-0.17}$	$2.3^{+1.1}_{-0.9}$	$0.40^{+0.22}_{-0.16}$	131^{+87}_{-80}		$1.11^{+0.03}_{-0.03}$	259/323
1+2	$1.77^{+0.05}_{-0.04}$	$3.80^{+0.08}_{-0.21}$	$6.38^{+0.02}_{-0.02}$	$0.9^{+0.2}_{-0.2}$	50^{+19}_{-17}	$6.22^{+0.16}_{-0.19}$	$2.7^{+0.9}_{-0.7}$	$0.54^{+0.27}_{-0.15}$	150^{+66}_{-64}		$1.11^{+0.03}_{-0.03}$	294/358
+PIN	$1.88^{+0.10}_{-0.05}$	$4.18^{+0.60}_{-0.16}$	$6.37^{+0.03}_{-0.01}$	$0.9^{+0.2}_{-0.2}$	44^{+17}_{-18}	$6.14^{+0.24}_{-0.31}$	$1.6^{+1.6}_{-0.9}$	$0.54^{+0.35}_{-0.23}$	< 158	$1.3^{+0.8}_{-0.3}$	$1.11^{+0.03}_{-0.03}$	295/374

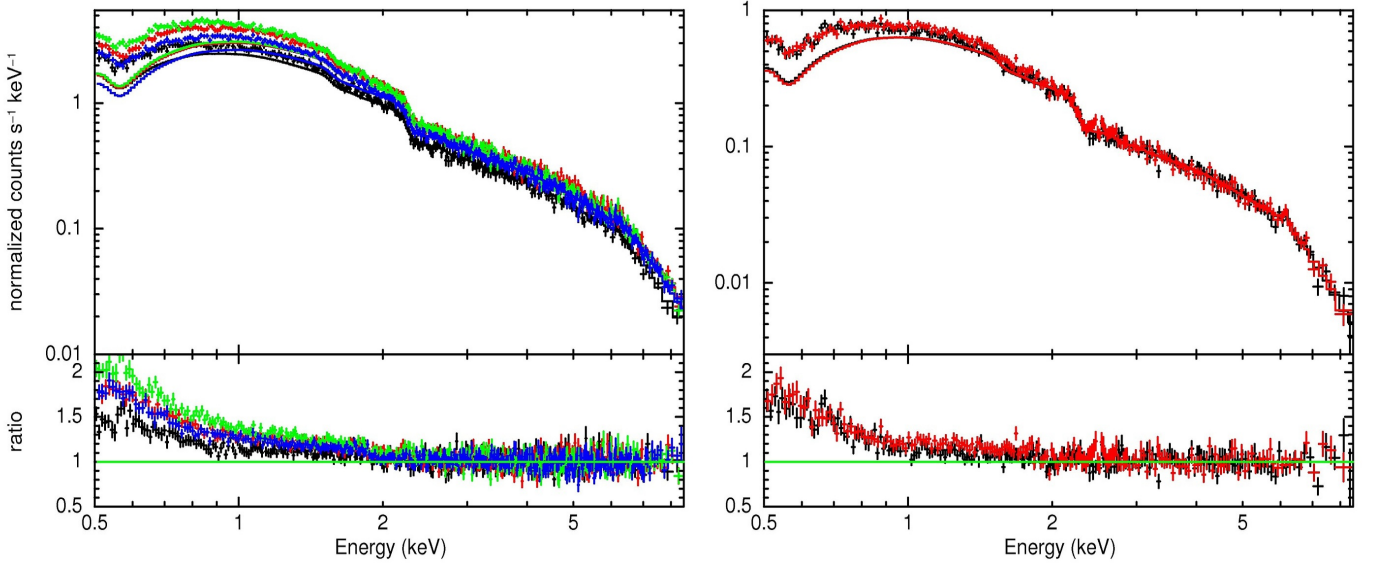


Figure 5. Mrk 509 (left) and Mrk 841 (right) soft excess: data from 3 to 10 keV are fitted with a power law plus three gaussian emission lines (see Table 2), and the model is then extrapolated to lower energies. Galactic absorption is taken into account. Only *XIS1* data are shown, as they extend down to 0.5 keV, but the analysis has been performed using both *FI* and *XIS1* data; the colour code for the different observations is as in Fig. 3. The energy on the abscissa is in the observer frame. The data have been rebinned for clarity purposes.

observation; the bottom panel shows the data-to-model ratio. The galactic absorption has been taken into account following Dickey & Lockman (1990), using $N_H = 4.11 \cdot 10^{20} \text{cm}^{-2}$ for Mrk 509 and $N_H = 2.34 \cdot 10^{20} \text{cm}^{-2}$ for Mrk 841. The soft excess shape is remarkably similar for the two Seyfert galaxies, and for Mrk 509 a spectral variability is observed at low energies.

As first qualitative study, we model the 0.5-10 keV spectrum with a broken power law (plus three gaussian emission lines,

with parameters fixed as in Table 2, and galactic absorption, fixed at values given above) in order to evaluate soft excess slope (Γ_s) and energy break E_b . As shown in Table 3, this model does not give a good fit to our data : the soft spectrum between 0.5 and 3 keV shows clear signature of curvature and cannot be described by a power law.

3.3. Hard Excess

Extrapolating the 3-10 keV best fit power law to high energies, considering *PIN* data, a hard excess appears as well. This feature is well explained by introducing a distant reflection by cold material, which accounts at the same time for the Fe $K\alpha$ narrow emission line and the high energy bump. In order to quantify the amount of reflected emission required, we fitted the summed *PIN* and *XIS* (above 3 keV) data with a power law (plus three gaussian lines, as described in the previous section) plus *pexrav* (Magdziarz & Zdziarski 1995), a model which describes reflection from neutral material. *Pexrav* free parameters are the reflection scaling factor R_{pexrav} (which is equal to 1 for a source isotropically illuminating the disc); the illuminating power law high energy cut-off E_c (frozen at 100 keV); the abundances (fixed equal to solar values) and the disc inclination angle θ (frozen at 30 degrees). For the summed spectra we obtain $R_{pexrav} = 0.4^{+0.2}_{-0.2}$ and $1.3^{+0.8}_{-0.3}$ for Mrk 509 and Mrk 841, respectively. Adding the neutral reflection component slightly modifies the best fit parameters of the broad Fe emission line, in particular its equivalent width. Best fit parameters are given in Table 2. *Pexrav* has the advantage that it gives directly the information about the reflected fraction R_{pexrav} , but it does not evaluate the narrow Fe $K\alpha$ emission line produced. We then decided to use *reflext*, a modified (and not public) version of *reflion* model (an older version of *reflionx* (Ross et al. 1999; Ross & Fabian 2005); see section 3.6). Unlike *reflion*, in which the ionisation parameter ξ is comprised between 10 and 10^4 erg cm s $^{-1}$, in *reflext* the ξ parameter space has been extended as low as 1 erg cm s $^{-1}$. Using *reflext* the evaluation of the reflected fraction is less accessible, but the Fe $K\alpha$ narrow emission line and the high energy bump are intrinsically tied. In the following we add *reflext* with parameters $Fe/Fe_{\odot} = 1$, $\Gamma_{reflext} = \Gamma$ and $\xi = 1$ erg cm s $^{-1}$. Its normalization parameter $C_{reflext}$ has been frozen in order that the flux of the model in the narrow Fe $K\alpha$ emission line reproduces the observed line flux. As the intensity of the reflected emission depends on the slope of the illuminating continuum, we evaluated the value of $C_{reflext}$ which reproduces the observed line flux as a function of Γ ; we fitted the result with a polynomial function, and we fixed the *reflext* normalization as a function of Γ .

3.4. Fe $K\alpha$ narrow emission line in Mrk 841

We present here the analysis of the Fe $K\alpha$ emission line in Mrk 841. Ponti et al. (2009) already presented a thorough study of the iron K complex in Mrk 509.

A narrow ($\sigma = 0$) Fe $K\alpha$ emission line has been observed in past Mrk 841 observations, and, in particular, P07 claimed that this narrow component is roughly constant in time, in agreement with a remote reflection scenario. We tested this hypothesis fitting the 3-10 keV *XIS* data with a power law plus a narrow Gaussian emission line, with σ fixed to zero, as done by P07. In Fig. 6 we report the contour plots of line flux versus line energy, for the two *Suzaku* observations, and we compare them to P07 results (*XMM/Newton*, observations from 2001 to 2005). The line flux is in agreement with what had been found by P07, and no variability is observed. Line energy, in the source frame, is consistent with iron $K\alpha$ for both observations.

In the following we concentrate on the broad band spectral fitting of Mrk 509 and Mrk 841 data with three different physical models : a double Comptonisation, a blurred reflection and

Table 3. Best fit parameter values for the broken power law model. *XIS/FI* data between 0.6 and 10 keV and *XIS1* data between 0.5 and 8.5 keV have been considered. The power law normalization C_h is the number of photons keV $^{-1}$ cm $^{-2}$ s $^{-1}$ at 1 keV.

Mrk 509					
Obs.	Γ_s	E_b (keV)	Γ_h	$C_h(10^{-3})$	χ^2/DOF
1	$2.24^{+0.08}_{-0.05}$	$1.02^{+0.07}_{-0.09}$	$1.87^{+0.01}_{-0.01}$	$13.8^{+0.2}_{-0.4}$	743/726
2	$2.16^{+0.02}_{-0.02}$	$1.83^{+0.09}_{-0.08}$	$1.86^{+0.01}_{-0.01}$	$18.0^{+0.1}_{-0.1}$	849/677
3	$2.29^{+0.01}_{-0.01}$	$1.74^{+0.06}_{-0.07}$	$1.93^{+0.01}_{-0.01}$	$19.3^{+0.1}_{-0.1}$	902/652
4	$2.12^{+0.01}_{-0.01}$	$1.96^{+0.09}_{-0.10}$	$1.84^{+0.01}_{-0.01}$	$15.6^{+0.1}_{-0.1}$	936/689
2+3+4	$2.19^{+0.01}_{-0.01}$	$1.77^{+0.04}_{-0.04}$	$1.89^{+0.01}_{-0.01}$	$17.3^{+0.1}_{-0.1}$	1248/721
Mrk 841					
Obs.	Γ_s	E_b (keV)	Γ_h	$C_h(10^{-3})$	χ^2/DOF
1	$2.44^{+0.06}_{-0.08}$	$1.02^{+0.06}_{-0.04}$	$1.82^{+0.01}_{-0.01}$	$4.09^{+0.07}_{-0.07}$	686/651
2	$2.40^{+0.09}_{-0.08}$	$0.96^{+0.06}_{-0.04}$	$1.87^{+0.01}_{-0.01}$	$4.21^{+0.12}_{-0.13}$	604/613
1+2	$2.44^{+0.06}_{-0.06}$	$1.00^{+0.04}_{-0.03}$	$1.85^{+0.01}_{-0.01}$	$4.18^{+0.08}_{-0.08}$	804/694

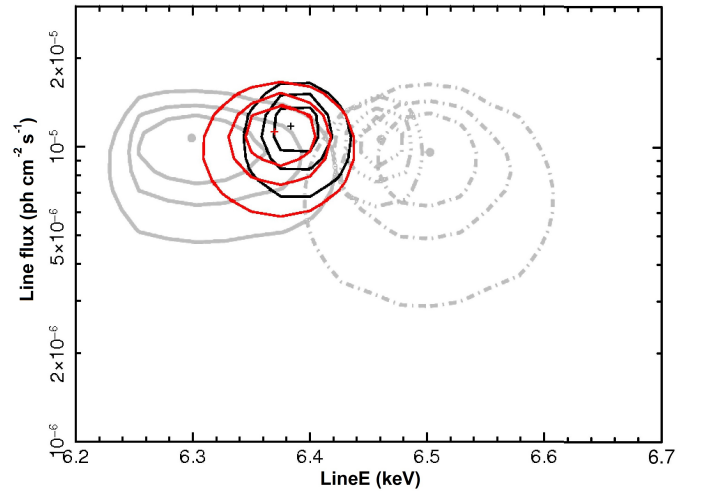


Figure 6. Contour plots (in black for obs.1, and in red for obs.2) of line flux versus line energy (source frame) for the narrow emission Gaussian line in Mrk 841. The three confidence levels are for 68, 90 and 99%, respectively. In grey are superimposed the contour plots of 2001-2005 *XMM/Newton* observations (see P07, Fig. 9).

a smeared absorption. As only weak flux variability is observed between individual Mrk 509 observations, and as no significant variability is observed between individual Mrk 841 observations, we perform and discuss the broad band spectral analysis for the summed spectra only (unless explicitly mentioned).

3.5. Double Comptonisation model

In the standard disc-corona scenario (Haardt & Maraschi 1993), the power law high energy emission is explained as a Comptonisation of thermal photons emitted by the black hole accretion disc. Electrons producing this inverse Compton effect have temperature $kT_e \approx 100$ keV and low optical depth, $\tau \approx 1$. One possibility to easily explain the soft excess is that there is a second warm Comptonisation region, with lower temperature and higher optical depth, which modifies the black body emission from the accretion disc, scattering UV photons up to soft X-ray energies. A physical interpretation of this "second corona" can be a warm skin on the disc surface (Janiuk

et al. 2001), or a transition region between an outer disc and an optically thin inner flow (Magdziarz et al. 1998). We used *NTHComp* (Życki et al. 1999), part of *XSpec* models, to simulate Comptonised spectra: this model solves the Kompaneets equation, and the output spectrum is parametrised by the electron temperature kT_e and the spectral index Γ ; seed photons come from an accretion disc spectrum, parametrised by kT_{disc} , the temperature at the inner radius. The electron temperature of the corona producing the high energy emission (subscript h), kT_h , can be constrained only via the high energy cutoff: as we do not observe it in our data, we fixed it at 100 keV. For the soft Comptonisation region (subscript s), we cannot fit at the same time Γ_s and kT_s , and, following GD04, we fixed $\Gamma_s = 2$.

The exact value of kT_{disc} does not affect the fit as long as it is lower than our energy domain: we chose $kT_{disc} = 45$ eV. We added *reflex* to our model to describe the reflection from distant material, with normalization parameter frozen as described above, plus two gaussian functions for the Fe $K\beta$ and the Fe K_{broad} emission lines, as in Table 2 (for the *XIS* + *PIN* fit). Best fit results are given in Table 4.

The double Comptonisation model has been studied in detail by GD04: they fitted a sample of 26 AGN showing that the cold Comptonisation region has a remarkably constant temperature $< kT_s > = 0.12$ keV with $\sigma = 0.02$ keV, despite large variations in black hole mass and AGN luminosity. The model they used was *NTHComp*, too. The values we found for Mrk 509 and Mrk 841 during Suzaku observations are in agreement with their statistics. We remind here that the exact value of kT_s depends on the assumption done for Γ_s : the only physical parameter which can be constrained (when the high energy cut-off is not observed) is the Comptonisation parameter y , defined as $4kT/(mc^2) \cdot \text{Max}(\tau, \tau^2)$, where τ is the plasma optical depth. The Γ parameter represents the asymptotic power law function which describes the Comptonised spectrum, and can be expressed as $(2.25 + 4/y)^{0.5} - 0.5$, which is equal to 2 for $y = 1$. The most important result obtained by GD04 is not the exact value of kT_s , but its constancy in AGN samples.

Following GD04, we evaluated the soft excess strength, R_{GD} , defined as the ratio of the unabsorbed 0.3-2 keV flux in the cool and hot Comptonised components: it is equal to $0.23^{+0.04}_{-0.05}$ for Mrk 509 and $0.28^{+0.08}_{-0.04}$ for Mrk 841, setting our sources in the lowest part of the GD04 sample.

3.5.1. Additional contribution of the warm absorber

Considering the χ^2 values, the double Comptonisation model does not provide a good fit to data. In fact, for both sources, the presence of a warm absorber has been confirmed, and its features could explain residuals to the fit. The most complete studies on the warm absorber of these two objects have been done using *XMM/RGS* data by Smith et al. (2007) and Detmers et al. (2010) for Mrk 509, and by Longinotti et al. (2010) for Mrk 841.

Smith et al. detected a three-phase warm absorber in Mrk 509: a low ionisation component ($\log \xi \approx 0.89$ and column density $N_H \approx 7.9 \cdot 10^{20} \text{cm}^{-2}$), an intermediate ionisation phase ($\log \xi \approx 2.14$, $N_H \approx 7.5 \cdot 10^{20} \text{cm}^{-2}$) and a high ionisation one ($\log \xi \approx 3.26$, $N_H \approx 55 \cdot 10^{20} \text{cm}^{-2}$). Detmers et al. confirmed the presence of three different components in the warm absorber: they found a low ionisation phase ($\log \xi \approx 0.6$,

$N_H \approx 1.0 \cdot 10^{20} \text{cm}^{-2}$), an intermediate phase ($\log \xi \approx 1.95$, $N_H \approx 10.5 \cdot 10^{20} \text{cm}^{-2}$), and a high ionisation phase ($\log \xi \approx 3.2$, $N_H \approx 80.0 \cdot 10^{20} \text{cm}^{-2}$).

A multi-phase warm absorber has been found in Mrk 841, too, by Longinotti et al., with an intermediate ionisation component ($\log \xi \approx 1.5$ - 2.2 , $N_H \approx 12$ - $39 \cdot 10^{20} \text{cm}^{-2}$) and a higher ionisation phase ($\log \xi = 2.8$ - 3.3 and $N_H \approx 76$ - $300 \cdot 10^{20} \text{cm}^{-2}$).

We tested the presence of the warm absorber using the model *zxipcf* (Reeves et al. 2008), part of *XSpec* models, which has as free parameters the ionisation parameter $\log \xi$, the column density N_H , the covering factor f and the redshift z . We started our study by multiplying the double Comptonisation model by one *zxipcf* component, with $f = 1$ and $z = z_{object}$. For Mrk 509, we find $\log \xi_{WA} = 2.19^{+0.05}_{-0.05}$ and $N_{H,WA} = 17^{+2}_{-2} \cdot 10^{20} \text{cm}^{-2}$, values which are consistent with the intermediate ionisation phase found by Smith et al. and Detmers et al.. For Mrk 841, we find $\log \xi_{WA} = 2.3^{+0.1}_{-0.1}$ and $N_{H,WA} = 17^{+4}_{-4} \cdot 10^{20} \text{cm}^{-2}$, consistent with the intermediate ionisation phase in Longinotti et al.. Adding *zxipcf* always improves the goodness of the fit, as confirmed by a F-test: the null hypothesis probabilities are $7 \cdot 10^{-44}$ (for Mrk 509) and $1 \cdot 10^{-13}$ (for Mrk 841).

We then tried to add a second absorber (subscript 2). For Mrk 509, we find that a two-phase warm absorber is statistically preferred (the associated F-test probability is $5 \cdot 10^{-5}$) and we measure $\log \xi_{WA,2} = 2.7^{+0.4}_{-0.1}$, $N_{H,WA,2} = 7^{+9}_{-2} \cdot 10^{20} \text{cm}^{-2}$, $\log \xi_{WA,1} = 1.7^{+0.1}_{-0.1}$ and $N_{H,WA,1} = 8^{+2}_{-1} \cdot 10^{20} \text{cm}^{-2}$. For the high ionisation phase, *XMM/RGS* data showed also a warm absorber flow velocity blueshifted relatively to the galaxy: we then fixed $z_{WA,2}$ at the value found by Detmers et al. ($z_{WA,2} = 0.0334$, corresponding to $v = -290 \text{ km s}^{-1}$). For Mrk 841 adding a second absorber does not improve the goodness of the fit and the absorber parameters are badly constrained: we then fixed $\log \xi_{WA,2} = 3.3$, equal to the value measured by Longinotti et al. during the 2001 *XMM* observation of Mrk 841.

Best fit results are given in Table 4 and plotted in Figs. 7 and 8 (left panel). We tested the presence of a three-phase warm absorber in Mrk 509, but the goodness of the fit worsens, even fixing the warm absorbers parameters at the values measured by *XMM/RGS*.

Zxipcf can take into account a covering factor $f < 1$, to describe partial covering absorbers. We tested the effect of this parameter on a one-phase warm absorber. For Mrk 509, leaving f free to vary, it decreases down to 0.3, while $N_{H,WA}$ increases, reaching $3 \cdot 10^{22} \text{cm}^{-2}$; the new fit is statistically better than the one with $f = 1$ (the null hypothesis probability is equal to $1 \cdot 10^{-7}$). For Mrk 841 the best fit result is always consistent with $f = 1$ (we measure $f > 0.7$). Despite the better fit obtained with $f < 1$ for Mrk 509, we decided to use and study the $f = 1$ case in order to compare our results to *XMM/RGS* results (and for consistency between the analysis of our two sources). In any case there is a degeneracy between f and N_H , and leaving f free affects the values of ξ and T_s and, consequently, the physical interpretation of our results. In the next sections, we will always use $f = 1$, with a reminder that, for Mrk 509, thawing f always leads to a better fit.

In both sources, *XMM/RGS* data revealed an OVII emission line at $E \approx 0.56$ keV. We tested the presence of this emission adding a narrow ($\sigma = 0$) gaussian line to the model (the fit has been performed using data below 10 keV, without *reflex*, which produces an OVII emission line as well (see below)).

For Mrk 509 we find a significant better fit (F-test probability

$= 4 \cdot 10^{-9}$) for the fourth observation, while for the other observations and for the summed spectra the goodness of the fit is not improved. However, it should be noted that at 0.56 keV we do not have the *XIS/FI* detectors (which start at 0.6 keV), and that we are at the energy edge of *XIS1*: the energy resolution is quite low (the emission line is defined by one bin only) and we cannot confirm if this statistically significant improvement of the fit corresponds to a true emission line detection.

For Mrk 841, adding a gaussian OVII emission line does not improve the goodness of the fit in any individual observation or in the summed spectrum.

The origin of this emission line is thought to be the warm gas itself but, on the other hand, we expect OVII emission from colder reflection, too. In particular, Ebrero et al. (2010) showed, for the Seyfert 1 Mrk 279, that the *reflex* code (for $\log \xi < 1.43$) produces an OVII line emission flux which exceeds the observed OVII line flux by a factor of 10 or more. For Mrk 509 and Mrk 841, such excess is not present: the line flux produced by *reflex* (with $\log \xi = 0$) is equal to $2.1 \cdot 10^{-4} \text{ cm}^{-2} \text{ s}^{-1}$ for Mrk 509 (compared to $2.7 \cdot 10^{-4} \text{ cm}^{-2} \text{ s}^{-1}$ found by Detmers et al.), and to $7.2 \cdot 10^{-5} \text{ cm}^{-2} \text{ s}^{-1}$ for Mrk 841 (compared to $(6.4 \pm 5.3) \cdot 10^{-5} \text{ cm}^{-2} \text{ s}^{-1}$ found by Longinotti et al. in the January 2005 *XMM/RGS* observation).

GD04 performed their fits without testing the presence of a warm absorber in their data. Looking at Table 4 we can see that, adding *zxipcf*, kT_s increases from 0.13-0.14 keV to 0.19-0.21 keV, becoming only marginally consistent with GD04 results.

3.6. Blurred reflection model

The constancy and universality of soft excess temperature is difficult to explain in a double Comptonisation scenario, for objects across different black hole masses (GD04); instead it is expected if some atomic processes are at work. If the reflection from the accretion disc is ionised, and if emission lines are broadened by relativistic velocity near the black hole, this component can explain the soft excess as well. We used the *reflionx* model (Ross et al. 1999; Ross & Fabian 2005), convolved with the *kdblur* model (Laor 1991), to describe the disc ionised reflection. For the relativistic blurring we assumed $R_{in} = 1.235 R_G$ (the last stable orbit for a near extremal Kerr black hole with parameter $a = 0.998$, (Thorne 1974)), $R_{out} = 100 R_G$, $\theta = 30$ degrees, and disc emissivity index $\beta = 3$ (Laor 1991); for *reflionx* we fixed iron abundance equal to the solar value, leaving ξ and the normalization free. Following what we did in the previous section, we added a neutral reflection from distant material (*reflex*, with normalization parameter fixed as a function of Γ , as described in Section 3.3), a narrow gaussian line (for the Fe $K\beta$ emission line) and a two-phase warm absorber totally covering the source (*zxipcf*), with ionisation parameter and column density left free to vary within the error bars of the values found using a double comptonisation continuum (see Section 3.5.1). A broad emission feature around 6.4 keV is expected from the blurred reflection on the accretion disc, so no broad emission line has been included in the model. Best fit results are given in Table 5.

The R parameter, which gives information about the reflected flux fraction, as defined by C06, is the ratio of the unabsorbed reflected component (*reflionx*) flux on the total (excluding *reflex*) unabsorbed flux in the 0.3-12 keV energy band. For a flat disc illuminated by an isotropic source we evaluated a value of $R \approx 0.5$ for a high ionisation state ($\log \xi > 3.5$), while for

lower ionisations the reflection fraction decreases, reaching 0.4 for $\log \xi = 3$, 0.2 for $\log \xi = 2$ and 0.1 for $\log \xi = 1.5$.

This model is widely used in literature: C06 analysed a sample of 34 type 1 AGN, fitting their *XMM-Newton* observations with *reflion* model (an older version of *reflionx*). For the R parameter, they found one third of the sources having no power law component ($R = 1$), while in the rest of the sample R is almost constantly distributed between 0.25 and 0.8. Our values, comprised between 0.15 and 0.18, are quite low compared to this result. In particular, Mrk 841 is included in their sample, and they found $R = 0.67 \pm 0.17$. This value is different from what has been found by P07, in a dedicated paper on *XMM-Newton* observations, including the one studied by C06, for which they found $R = 0.3$ (in their paper P07 gave $R' = 0.3$, where R' is the reflected fraction evaluated in the energy band 0.1-1000 keV, and including warm absorption; we reevaluated R using their best fit parameters). In our model we have frozen all *kdblur* parameters. We tried to thaw β , but its best fit value is always consistent with 3. C06 performed their fits leaving all, but R_{out} , *kdblur* parameters free to vary: with such a large number of parameters, best fit values become less well constrained, with several parameters pegged at lower or higher limits (as can be seen in C06, Table 3) and a physical interpretation of these results can be misleading. P07 results for *XMM-Newton* observations of Mrk 841 were $1.59 \leq \Gamma \leq 2.45$, $2 \leq \log \xi \leq 2.5$ and $\beta \approx 4$ (but in one observation they found $\beta > 8.6$), with a reflection fraction R' varying between 0.30 and 0.43.

The best fit result for Mrk 509 is not good ($\chi^2 = 1.25$) and some residuals are clearly observed between 6 and 7 keV (see Fig. 9). First we tried to thaw the inner radius and the inclination angle of the accretion disc: the fit is significantly improved (F-test probability = $1 \cdot 10^{-4}$) and we measure $R_{in} < 1.7 R_G$ and $\theta = 38^{+2}_{-3}$ degrees. However, this cannot take into account all the residuals observed near the Fe $K\alpha$ line. An excess of emission in the Fe $K\alpha$ complex could be due to iron abundance higher than the solar value: we tried to thaw this parameter but the best fit results are always consistent with $\text{Fe}/\text{Fe}_\odot = 1$. Adding a broad gaussian line, the fit is significantly improved (the null hypothesis probability is 10^{-29}). We measure $E_{0,broad} = 6.9^{+0.1}_{-0.1}$ keV, $C_{broad} = 10^{+1}_{-1} \cdot 10^{-5} \text{ photons cm}^{-2} \text{ s}^{-1}$ and $\sigma_{broad} = 0.8^{+0.3}_{-0.2}$ keV, with an equivalent width of 255^{+85}_{-66} eV (see Table 5 and Fig. 7, middle panel).

For Mrk 841, a good fit to the data is already provided by the first model (all *kdblur* parameters frozen at the values described above, and absence of a broad emission line), but the fit is improved when θ is left free to vary, and we found $\theta = 41^{+3}_{-4}$ degrees (F-test probability equal to $4 \cdot 10^{-4}$). Adding a broad emission line at the Fe K complex energy does not improve the goodness of the fit (F-test probability = 0.1 compared to the fit with θ thawed) (see Table 5 and Fig. 8, middle panel).

3.7. Smeared absorption model

An alternative model to explain the soft excess is a relativistically smeared absorption: high velocities can blur all atomic features, producing a curved continuum spectrum. This absorption could represent an outflowing disc wind, as shown by Murray & Chiang (1997). We used *swind* (GD04), part of *XSpec* models, to describe this component: a *XSTAR* (Bautista & Kallman 2001) grid (calculated assuming $\Gamma = 2.4$ and micro-turbulent velocity of 100 km/s) is convolved with a Gaussian function with width $\sigma = v/c$. Free parameters of *swind* model

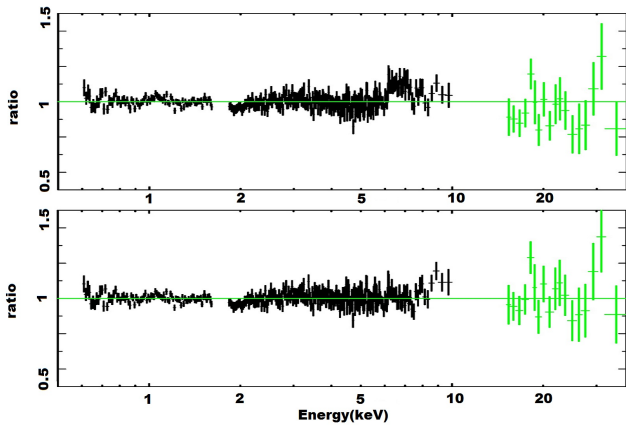


Figure 9. Ratio plot obtained for the fit of Mrk 509 data with a blurred reflection model with (bottom) or without (top) a broad emission $K\alpha$ line (see section 3.6). *XIS/FI* data are in black, while *HXD/PIN* data are in green. For clarity, the data have been rebinned, and *XIS1* data are not shown in this plot.

are the column density N_H , the ionisation parameter ξ and the velocity dispersion σ . As for the ionised reflection model, we added a neutral reflection (*reflect*), a narrow gaussian line for the Fe $K\beta$ emission line and a two-phase warm absorber (*zxipcf* model). As no broad Fe emission line is included in the model, we also added a broad emission line with parameters fixed as in Table 2 (for the *XIS + PIN* fit). Best fit results are shown in Table 6 and Figs. 7 and 8, right panel.

For both sources the values of σ are always pegged at the highest authorized value ($v = 0.5c$), and we can only give lower limits. It is interesting to cite the results of a fitting without *zxipcf*: σ decreases down to ≈ 0.3 (it is equal to $0.29^{+0.01}_{-0.02}$ and $0.28^{+0.03}_{-0.02}$ for Mrk 509 and Mrk 841, respectively). We can compare our results for Mrk 841 with P07, who tested the same model for *XMM-Newton* observations: their best fit values for *swind* model are $2.4 \leq \log \xi \leq 3.5$, $0.9 \leq N_H \leq 4.4 \cdot 10^{23} \text{cm}^{-2}$ and σ consistent with 0.3 (but > 0.4 in two cases). The values of N_H and ξ we found are in agreement with these results. This model has been studied by Middleton et al. (2007) (hereafter M07), who analysed the same AGN sample used by C06. They found that, in half of their sample, σ is pegged at 0.5, and that, in general, it has a typical value > 0.3 . Their ξ and N_H best fit values do not have large dispersion: $\log \xi$ varies between 2.5 and 3.7, with lower values ($\log \xi < 3$) for their Narrow-Line Seyfert 1 (NLS1) galaxy sample; N_H values are comprised between $5 \cdot 10^{22}$ and $5 \cdot 10^{24}$, with, once again, values lower than $1.5 \cdot 10^{23}$ restricted to NLS1 galaxies. The intrinsic power law spectral index varies between 2.0 and 3.4, with a clear difference between the softer NLS1s and the harder broad-line AGN. The values we found are in agreement with these global results, but Γ is only marginally compatible with M07's results. The evaluation of Γ is important since it affects the soft excess strength and shape, and then *swind* parameters. In order to test if *PIN* data have an effect in the evaluation of Γ , we tried to fit *XIS* data alone, but the best fit values of Γ are compatible with the broad band fit.

4. Discussion and Conclusions

Mrk 509 and Mrk 841 are two bright Seyfert 1 galaxies, well known for their soft X-ray excess, their iron $K\alpha$ emission line and their spectral variability. In this paper we presented the

analysis of new *Suzaku* observations: four of Mrk 509 (from April, 2006 to November, 2006), and two of Mrk 841 (January and July, 2007). The soft excess is clearly present in both sources, with a flux ≈ 2 times higher than the 3-10 keV power law extrapolation at 0.5 keV. Pounds & Reeves (2002) analysed a sample of six Seyfert 1 galaxies, showing that a variety of soft excess shapes exists, correlated with AGN luminosity: our sources during *Suzaku* observations can be described as 'Gradual Soft Excess' galaxies, according to Pounds and Reeves terminology. We can compare our results to past observations (Pounds et al. 2001; Pounds & Reeves 2002; De Rosa et al. 2004; P07): a soft excess 2 times higher than the power law extrapolation at 0.5 keV is common for both sources, even though Mrk 841 during *XMM-Newton* observations showed a stronger soft excess, 2.5-3 times higher than the power law, and the soft excess of Mrk 509 during obs.1 is quite low, similar to what was observed during the highest state in *BeppoSAX* observations (De Rosa et al. 2004).

Comparing our observations to statistical studies of the soft excess (GD04, C06, M07), we confirm that both sources have been detected during a weak soft excess state, setting them always in the lower part of the sample: for the double Comptonisation model, the "soft excess strength" (R_{GD} , as defined by GD04) of Mrk 509 and Mrk 841 during our observations is comprised between 0.23 and 0.28, while the GD04 sample has a typical value of 0.4-0.6; in the reflection model, we found a R parameter comprised between 0.15 and 0.18, quite low compared to the reflected flux fractions of C06.

Both sources show a hard excess at energies greater than 10 keV. This excess is weak compared to what has been observed by *Suzaku* in three other Seyfert 1 galaxies (Walton et al. 2010), though they are rather extreme examples of hard excesses.

A narrow Fe $K\alpha$ emission line is detected in both sources, consistent with a reflection by remote and cold material (i.e. the dust torus or the furthest regions of the accretion disc). For Mrk 841 we compared our results to previous *XMM-Newton* observations, showing that the line flux is constant in time. For Mrk 509 Fe K complex emission, we refer to Ponti et al. (2009). A broad Fe K emission line is observed as well, with equivalent width ≈ 150 eV in both sources.

We detected a two-phase warm absorber in Mrk 509 data, with $\log \xi_{\text{WA},1} \approx 1.7$ and $\log \xi_{\text{WA},2} \approx 2.7$, values which are lower than what have been found by Smith et al. and Detmers et al.. We do not see in the *Suzaku* data the low ionisation phase ($\log \xi = 0.6 - 0.9$) of the absorber detected by *XMM/RGS*. For Mrk 841 we found a low ionisation warm absorber with $\log \xi_{\text{WA},1} \approx 2.2$, consistent with the lower ionisation phase in the two-phase absorber described by Longinotti et al. (2010), and we froze the high ionisation parameter $\log \xi_{\text{WA},2} = 3.3$. For Mrk 509, considering a warm absorber covering factor lower than 1, always improves the fit.

We started the analysis of the broad band spectra of the two sources considering the double Comptonisation model: it correctly fits the data ($\chi^2 \approx 1.09$ for Mrk 509, and $\chi^2 \approx 1.00$ for Mrk 841), but the constancy of the temperature of the cold Comptonisation region in statistical studies of Seyfert 1 galaxies is not explained by current physical models of accretion disk atmospheres, and thus disfavors this model.

We then fitted the broad band spectrum with the two competitive

models aimed to explain the soft excess with atomic processes: a blurred reflection and a smeared ionised absorption.

For Mrk 509, we need to add a broad emission line in order to correctly fit the data, and we obtain $\chi^2 \approx 1.04$ -1.02 for the blurred reflection and the smeared absorption model, respectively.

The physical origin of this emission is not clear: for the reflection model, a broadened emission line is already included in the code we used, and it is difficult to explain why we do need some more reflection at $E \approx 6.4$ keV. Interestingly, this result suggests that the reflection model correctly describes the soft excess shape and strength, but it underestimates the broad emission at Fe K complex energies.

For the smeared absorption model we do not include any reflection from the accretion disc, and the fact that we need to add a broad emission line is less critical: the *swind* code assume a simple power law emission as input for the smeared absorption, and the presence of residuals in the Fe K complex region means that the continuum spectrum absorbed by the wind does include, indeed, some reflected component.

For Mrk 841 no extra-emission in the reflection model is required, while a broad gaussian emission line is needed in the absorption model: each model gives a good fit to the data, and none of them can be invalidated ($\chi^2 \approx 1.04$ for the two models).

Suzaku data, characterised by a good energy resolution in a large energy domain (0.5-60 keV), seemed to be able to constrain the intrinsic power law photon index at high energies, and then to favor one model over another. The best fit models show that, while in the soft X-ray domain the models are degenerate, in the hard energy band they do not superpose any more and we could, in principle, distinguish between them, but the *PIN* signal-to-noise ratio is still too low to constrain the fit. For the sum of Mrk 509 observations, we can estimate from the best fit model in the hard X-ray domain a flux $F_{17-60\text{keV}} = 4.47, 4.81$ and $4.27 \cdot 10^{-11}$ ergs cm $^{-2}$ s $^{-1}$ and $F_{14-150\text{keV}} = 7.64, 8.07$ and $7.66 \cdot 10^{-11}$ ergs cm $^{-2}$ s $^{-1}$ for the double Comptonisation, the blurred reflection and the smeared absorption model, respectively; for the sum of Mrk 841 observations we obtain $F_{17-60\text{keV}} = 1.94, 2.15$ and $1.67 \cdot 10^{-11}$ ergs cm $^{-2}$ s $^{-1}$ and $F_{14-150\text{keV}} = 3.47, 3.72$ and $3.06 \cdot 10^{-11}$ ergs cm $^{-2}$ s $^{-1}$ for the three models, respectively. These values can be compared with the *INTEGRAL* (Krivonos et al. 2010) and *Swift/BAT* (Cusumano et al. 2010) detections of our sources: *INTEGRAL* detected Mrk 509 at $F_{17-60\text{keV}} = 5.90 \cdot 10^{-11}$ ergs cm $^{-2}$ s $^{-1}$ and Mrk 841 at $F_{17-60\text{keV}} = 3.07 \cdot 10^{-11}$ ergs cm $^{-2}$ s $^{-1}$; *Swift/BAT* observed a flux in the 14-150 keV energy band equal to $8.5 \cdot 10^{-11}$ ergs cm $^{-2}$ s $^{-1}$ for Mrk 509 and $2.9 \cdot 10^{-11}$ ergs cm $^{-2}$ s $^{-1}$ for Mrk 841. The differences in the predicted high-energy fluxes show that a simultaneous broad band observation with adequate signal-to-noise ratio would be able to distinguish between the different models.

Statistical studies of AGN can help in solving the problem of the origin of the soft excess. The discovery of the remarkably constant temperature of the cold Comptonisation region, despite the fact that AGN luminosity and black hole mass span several decades, is hardly explained in a double Comptonisation scenario. Our kT_s values are in agreement with GD04 results, but it is interesting to note that adding a warm absorber (which was not included in GD04 analysis) affects kT_s best fit values.

Reflection and absorption models, linked to atomic processes, can easily explain the low spread in the soft excess temperature. However, the smeared absorption model has the weakness that the velocity dispersion required to fit the soft excess is very high, reaching $c/2$, which corresponds to extremely relativis-

tic terminal velocities for the wind. Numerical simulations (Schurch & Done 2008) show that disc winds have $\sigma < 0.1c$, very low compared to *swind* model results. An outlet could be a magnetically driven wind, partially covering the source. It is important to underline that *swind* takes into account only the absorption by the wind, but if we consider its emission, too, (Chevallier et al. 2006; Schurch & Done 2006) the fit requires a lower smearing velocity and a lower column density. A possible concern of the *swind* model is that the absorption is evaluated assuming an incident power law spectrum with $\Gamma = 2.4$, not consistent with the Γ best fit values of our observations.

The Fe broad line excess we observe in both sources suggests that, even in an absorption scenario, we need some reflected emission from the inner regions of the accretion disc. A broad Fe K emission line can also be reproduced by recent disk wind models (Sim et al. 2010), with lower outflow velocity (0.1c).

The blurred reflection model fits the *Suzaku* data well for Mrk 841, while for Mrk 509 we need an extra-emission at Fe K energies, which is difficult to explain. The model does not need a high reflection fraction R , seen in several other cases, which may be explained by a huge light bending effect (Miniutti & Fabian 2004) close to the black hole.

It is of course possible that different processes are at work at the same time : in this scenario (which is difficult to test in a stationary framework due to the high number of free parameters involved) the broad emission observed in Mrk 509 could be due to standard ionised reflection on the accretion disc, while Comptonisation or smeared absorption should be responsible for the soft excess below 1 keV (see Patrick et al. (2011)).

Alternatively, the continuum X-ray emission from the hot corona can deviate from a powerlaw when measured over a broad energy band, showing an intrinsic curvature which has not been taken into account in our modeling.

Variability studies can disentangle different models: in the blurred reflection scenario, variability can be explained by changes in the height of the corona above the disc, but this picture implies a strong continuum-reflected component correlation which has not been observed. In the smeared absorption model, spectral variability is more easily explained by variation in the absorber physical parameters, or in its covering factor. Unluckily, neither of our sources showed a strong variability during *Suzaku* observations, and we could not use temporal information to better constrain our models.

Future X-ray observatories, and in particular *Astro-H* (Takahashi et al. 2010) and *NuSTAR* (Harrison et al. 2010), with higher sensibility and energy resolution in the hard X-ray domain, will be able to better constrain the spectrum, casting light on the physical origin of the soft excess in Seyfert 1 galaxies.

5. Acknowledgments

This research has made use of data obtained from the *Suzaku* satellite, a collaborative mission between the space agencies of Japan (JAXA) and the USA (NASA). This work has been financially supported by the GdR PCHE in France. MC thanks Matteo Guainazzi for useful discussion and for the help given in the rebinning of the data. GP acknowledges support via an EU Marie Curie Intra-European Fellowship under contract no. FP7-PEOPLE-2009-IEF-254279. POP acknowledges financial support from the CNES agency. We also thank the anonymous referee for having provided constructive remarks and improved the contents of the paper.

References

- Abdo, A. A., Ackermann, M., Ajello, M., et al. 2010, *ApJ*, 710, 810
- Akiyama, M., Ueda, Y., Ohta, K., Takahashi, T., & Yamada, T. 2003, *ApJS*, 148, 275
- Arnaud, K. A., Branduardi-Raymont, G., Culhane, J. L., et al. 1985, *MNRAS*, 217, 105
- Bautista, M. A. & Kallman, T. R. 2001, *ApJS*, 134, 139
- Bianchi, S., Matt, G., Haardt, F., et al. 2001, *A&A*, 376, 77
- Boldt, E. & Leiter, D. 1987, *ApJ*, 322, L1
- Chevallier, L., Collin, S., Dumont, A., et al. 2006, *A&A*, 449, 493
- Cooke, B. A., Ricketts, M. J., Maccacaro, T., et al. 1978, *MNRAS*, 182, 489
- Crummy, J., Fabian, A. C., Gallo, L., & Ross, R. R. 2006, *MNRAS*, 365, 1067
- Cusumano, G., La Parola, V., Segreto, A., et al. 2010, *A&A*, 524, A64+
- Czerny, B., Nikolajuk, M., Róžańska, A., et al. 2003, *A&A*, 412, 317
- Dadina, M., Cappi, M., Malaguti, G., Ponti, G., & de Rosa, A. 2005, *A&A*, 442, 461
- de La Calle Pérez, I., Longinotti, A. L., Guainazzi, M., et al. 2010, *A&A*, 524, A50+
- De Rosa, A., Piro, L., Matt, G., & Perola, G. C. 2004, *A&A*, 413, 895
- Detmers, R. G., Kaastra, J. S., Costantini, E., et al. 2010, *A&A*, 516, A61+
- Dickey, J. M. & Lockman, F. J. 1990, *ARA&A*, 28, 215
- Done, C., Gierliński, M., & Kubota, A. 2007, *A&A Rev.*, 15, 1
- Ebrero, J., Costantini, E., Kaastra, J. S., et al. 2010, *A&A*, 520, A36+
- Fisher, K. B., Huchra, J. P., Strauss, M. A., et al. 1995, *ApJS*, 100, 69
- George, I. M., Nandra, K., Fabian, A. C., et al. 1993, *MNRAS*, 260, 111
- George, I. M., Nandra, K., Turner, T. J., & Celotti, A. 1994, *ApJ*, 436, L59
- Gierliński, M. & Done, C. 2004, *MNRAS*, 349, L7
- Haardt, F. & Maraschi, L. 1993, *ApJ*, 413, 507
- Harrison, F. A., Boggs, S., Christensen, F., et al. 2010, in *Society of Photo-Optical Instrumentation Engineers (SPIE) Conference Series*, Vol. 7732, *Society of Photo-Optical Instrumentation Engineers (SPIE) Conference Series*
- Janiuk, A., Czerny, B., & Madejski, G. M. 2001, *ApJ*, 557, 408
- Kaastra, J. S., Petrucci, P. O., Cappi, M., et al. 2011, *ArXiv e-prints*
- Koyama, K., Tsunemi, H., Dotani, T., et al. 2007, *PASJ*, 59, 23
- Krivonos, R., Tsygankov, S., Revnivtsev, M., et al. 2010, *A&A*, 523, A61+
- Laor, A. 1991, *ApJ*, 376, 90
- Longinotti, A. L., Costantini, E., Petrucci, P. O., et al. 2010, *A&A*, 510, A92+
- Magdziarz, P., Blaes, O. M., Zdziarski, A. A., Johnson, W. N., & Smith, D. A. 1998, *MNRAS*, 301, 179
- Magdziarz, P. & Zdziarski, A. A. 1995, *MNRAS*, 273, 837
- Middleton, M., Done, C., & Gierliński, M. 2007, *MNRAS*, 381, 1426
- Miniutti, G. & Fabian, A. C. 2004, *MNRAS*, 349, 1435
- Miniutti, G., Ponti, G., Greene, J. E., et al. 2009, *MNRAS*, 394, 443
- Miyazawa, T., Haba, Y., & Kunieda, H. 2009, *PASJ*, 61, 1331
- Morini, M., Lipani, N. A., & Molteni, D. 1987, *ApJ*, 317, 145
- Murray, N. & Chiang, J. 1997, *ApJ*, 474, 91
- Palmeri, P., Mendoza, C., Kallman, T. R., Bautista, M. A., & Meléndez, M. 2003, *A&A*, 410, 359
- Patrick, A. R., Reeves, J. N., Porquet, D., et al. 2011, *MNRAS*, 411, 2353
- Perola, G. C., Matt, G., Fiore, F., et al. 2000, *A&A*, 358, 117
- Petrucci, P. O., Ponti, G., Matt, G., et al. 2007, *A&A*, 470, 889
- Piconcelli, E., Jimenez-Bailón, E., Guainazzi, M., et al. 2005, *A&A*, 432, 15
- Ponti, G., Cappi, M., Vignali, C., et al. 2009, *MNRAS*, 394, 1487
- Ponti, G., Miniutti, G., Cappi, M., et al. 2006, *MNRAS*, 368, 903
- Pounds, K. & Reeves, J. 2002, *ArXiv:astro-ph/0201436*, *Proceedings of the Symposium on 'New Visions of the X-ray Universe in the XMM-Newton and Chandra Era'*, 26-30 November 2001, ESTEC, The Netherlands
- Pounds, K., Reeves, J., O'Brien, P., et al. 2001, *ApJ*, 559, 181
- Pounds, K. A., Nandra, K., Fink, H. H., & Makino, F. 1994, *MNRAS*, 267, 193
- Pravdo, S., Nugent, J., Nousek, J., et al. 1981, *ApJ*, 251, 501
- Reeves, J., Done, C., Pounds, K., et al. 2008, *MNRAS*, 385, L108
- Reynolds, C. S. 1997, *MNRAS*, 286, 513
- Ross, R. R. & Fabian, A. C. 2005, *MNRAS*, 358, 211
- Ross, R. R., Fabian, A. C., & Young, A. J. 1999, *MNRAS*, 306, 461
- Sazonov, S., Revnivtsev, M., Krivonos, R., Churazov, E., & Sunyaev, R. 2007, *A&A*, 462, 57
- Schurch, N. J. & Done, C. 2006, *MNRAS*, 371, 81
- Schurch, N. J. & Done, C. 2008, *MNRAS*, 386, L1
- Shakura, N. I. & Sunyaev, R. A. 1976, *MNRAS*, 175, 613
- Sim, S. A., Miller, L., Long, K. S., Turner, T. J., & Reeves, J. N. 2010, *MNRAS*, 404, 1369
- Singh, K. P., Garmire, G. P., & Nousek, J. 1985, *ApJ*, 297, 633
- Singh, K. P., Westergaard, N. J., Schnopper, H. W., Awaki, H., & Tawara, Y. 1990, *ApJ*, 363, 131
- Smith, H. E., Burbidge, E. M., Baldwin, J. A., et al. 1977, *ApJ*, 215, 427
- Smith, R. A. N., Page, M. J., & Branduardi-Raymont, G. 2007, *A&A*, 461, 135
- Sobolewska, M. A. & Done, C. 2007, *MNRAS*, 374, 150
- Takahashi, T., Abe, K., Endo, M., et al. 2007, *PASJ*, 59, 35
- Takahashi, T., Mitsuda, K., Kelley, R., et al. 2010, in *Society of Photo-Optical Instrumentation Engineers (SPIE) Conference Series*, Vol. 7732, *Society of Photo-Optical Instrumentation Engineers (SPIE) Conference Series*
- Thorne, K. S. 1974, *ApJ*, 191, 507
- Turner, T. J. & Miller, L. 2009, *A&A Rev.*, 17, 47
- Walton, D. J., Reis, R. C., & Fabian, A. C. 2010, *MNRAS*, 1054
- Watanabe, C., Ohta, K., Akiyama, M., & Ueda, Y. 2004, *ApJ*, 610, 128
- Zycki, P. T., Done, C., & Smith, D. A. 1999, *MNRAS*, 309, 561

Table 4. Best fit parameter values for the double Comptonisation model, with (second row) or without (first row) a two-phase warm absorber. Γ_S and kT_H are frozen at values 2 and 100 keV, respectively. Distant reflection is modelled using *reflex*, whose normalisation parameter is frozen in order to reproduce the observed Fe $K\alpha$ line (see Section 3.3). Two gaussian functions are included in the model, for the narrow Fe $K\beta$ and the broad Fe K emission line, with parameters frozen as in Table 2. *NTHComp* normalization parameters C are in units of $\text{keV}^{-1} \text{cm}^{-2} \text{s}^{-1}$ at 1 keV; warm absorber column density N_H is given in units of cm^{-2} , and ionisation parameter ξ in units of erg cm s^{-1} . Frozen parameters are marked by (F). The last two columns give the chi squared value over the number of degrees of freedom and the associated probability.

Mrk 509										
Obs.	kT_S (keV)	C_S (10^{-3})	Γ_H	C_H (10^{-3})	$N_{H,WA,1}$ (10^{20})	$\log \xi_{WA,1}$	$N_{H,WA,2}$ (10^{20})	$\log \xi_{WA,2}$	χ^2/DOF	prob
2+3+4	$0.127^{+0.006}_{-0.003}$	$0.9^{+0.2}_{-0.1}$	$1.96^{+0.01}_{-0.01}$	$15.8^{+0.1}_{-0.1}$	-	-	-	-	1077/737	$3 \cdot 10^{-15}$
2+3+4	$0.206^{+0.005}_{-0.006}$	$3.8^{+0.2}_{-0.2}$	$1.92^{+0.01}_{-0.01}$	$15.1^{+0.2}_{-0.2}$	8^{+2}_{-1}	$1.7^{+0.1}_{-0.1}$	7^{+9}_{-2}	$2.7^{+0.4}_{-0.1}$	800/733	0.04
Mrk 841										
Obs.	kT_S (keV)	C_S (10^{-3})	Γ_H	C_H (10^{-3})	$N_{H,WA,1}$ (10^{20})	$\log \xi_{WA,1}$	$N_{H,WA,2}$ (10^{20})	$\log \xi_{WA,2}$	χ^2/DOF	prob
1+2	$0.137^{+0.13}_{-0.06}$	$0.35^{+0.10}_{-0.05}$	$1.82^{+0.01}_{-0.01}$	$4.00^{+0.04}_{-0.08}$	-	-	-	-	769/707	0.005
1+2	$0.19^{+0.01}_{-0.01}$	$0.85^{+0.11}_{-0.11}$	$1.80^{+0.01}_{-0.01}$	$3.92^{+0.06}_{-0.07}$	14^{+4}_{-7}	$2.2^{+0.2}_{-0.3}$	< 41	3.3 (F)	705/704	0.48

Table 5. Best fit parameter values for the blurred reflection model. Distant reflection is modelled using *reflex*, whose normalisation parameter is frozen in order to reproduce the observed narrow Fe $K\alpha$ line (see Section 3.3). A gaussian function is included in the model, for the narrow Fe $K\beta$ emission line, with parameters frozen as in Table 2. For Mrk 509, the best fit results including a broad gaussian emission line are also shown. *reflionx* and power law normalization parameters C are in units of $\text{keV}^{-1} \text{cm}^{-2} \text{s}^{-1}$ at 1 keV; ionisation parameter ξ is given in units of erg cm s^{-1} ; the line normalization parameter C_{broad} is the integrated number of photons $\text{cm}^{-2} \text{s}^{-1}$ in the line; σ is the line width expressed in keV. The R parameter is defined as the ratio of the flux of the unabsorbed reflected component on the total unabsorbed flux (evaluated between 0.3 and 12 keV). The two-phase warm absorber parameters are constrained within the range evaluated with the double Comptonisation model (Table 4). The last two columns give the chi squared value over the number of degrees of freedom and the associated probability.

Mrk 509										
Obs.	Γ	$C(10^{-3})$	$\log \xi$	$C_{reflionx}(10^{-6})$	$E_{broad}(keV)$	$C_{broad}(10^{-5})$	$\sigma_{broad}(keV)$	R	χ^2/DOF	prob
2+3+4	$2.041^{+0.004}_{-0.004}$	$15.9^{+0.1}_{-0.1}$	$1.54^{+0.14}_{-0.06}$	$11.5^{+2.2}_{-2.9}$	-	-	-	$0.16^{+0.03}_{-0.04}$	915/733	$5 \cdot 10^{-6}$
2+3+4	$2.039^{+0.007}_{-0.005}$	$15.9^{+0.1}_{-0.1}$	$1.73^{+0.03}_{-0.02}$	$6.1^{+0.7}_{-1.1}$	$6.9^{+0.1}_{-0.1}$	10^{+1}_{-1}	$0.8^{+0.3}_{-0.2}$	$0.15^{+0.01}_{-0.02}$	756/730	0.25
Mrk 841										
Obs.	Γ	$C(10^{-3})$	$\log \xi$	$C_{reflionx}(10^{-6})$	$E_{broad}(keV)$	$C_{broad}(10^{-5})$	$\sigma_{broad}(keV)$	R	χ^2/DOF	prob
1+2	$1.89^{+0.02}_{-0.01}$	$3.9^{+0.1}_{-0.1}$	$1.80^{+0.09}_{-0.05}$	$1.9^{+0.04}_{-0.05}$	-	-	-	$0.18^{+0.04}_{-0.05}$	730/704	0.24

Table 6. Best fit parameter values for the smeared absorption model. Distant reflection is modelled using *reflex*, whose normalisation parameter is frozen in order to reproduce the observed Fe $K\alpha$ line (see Section 3.3). For both sources, two gaussian functions are included in the model, for the narrow Fe $K\beta$ and the broad Fe K emission line, with parameters frozen as in Table 2. Power law normalization parameter C is in units of $\text{keV}^{-1} \text{cm}^{-2} \text{s}^{-1}$ at 1 keV; wind column density N_H is given in units of cm^{-2} , and ionisation parameter ξ in units of erg cm s^{-1} . The two-phase warm absorber parameters are constrained within the range evaluated with the double Comptonisation model (Table 4). The last two columns give the chi squared value over the number of degrees of freedom and the associated probability.

Mrk 509							
Obs.	Γ	$C(10^{-3})$	$N_H(10^{22})$	$\log \xi$	σ	χ^2/DOF	prob
2+3+4	$2.06^{+0.01}_{-0.01}$	$23.8^{+0.3}_{-0.5}$	18^{+2}_{-1}	$3.29^{+0.03}_{-0.02}$	> 0.45	748/732	0.33
Mrk 841							
Obs.	Γ	$C(10^{-3})$	$N_H(10^{22})$	$\log \xi$	σ	χ^2/DOF	prob
1+2	$1.97^{+0.02}_{-0.02}$	$6.25^{+0.07}_{-0.12}$	12^{+3}_{-3}	$3.10^{+0.10}_{-0.09}$	> 0.46	732/703	0.21

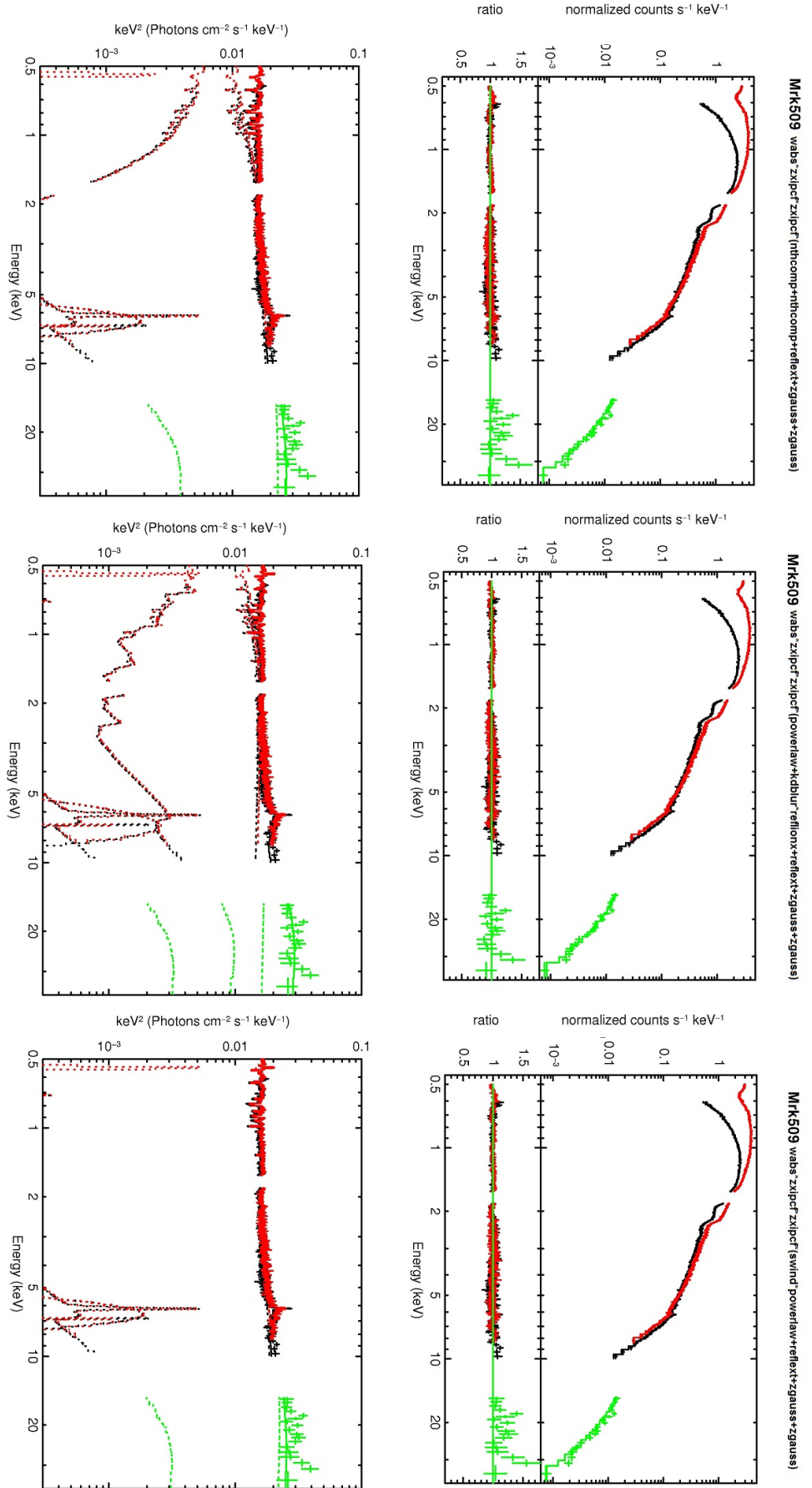


Figure 7. Top: Mrk 509 data (sum of *Suzaku* observations) and, in the subplot, data-to-model ratio. Bottom: unfolded data. Colour code for the different *Suzaku* instruments: *XIS/EP-black*, *XIS/-red* and *HXD/PIN-green*. Three different models are shown, from left to right: double Comptonisation, blurred reflection and smeared absorption. Solid lines correspond to the best fit model, and thin dashed lines to the model different components. For the three models a broad emission line component is required. The energy on the abscissa is in the observer frame. The data have been rebinned for clarity purposes.

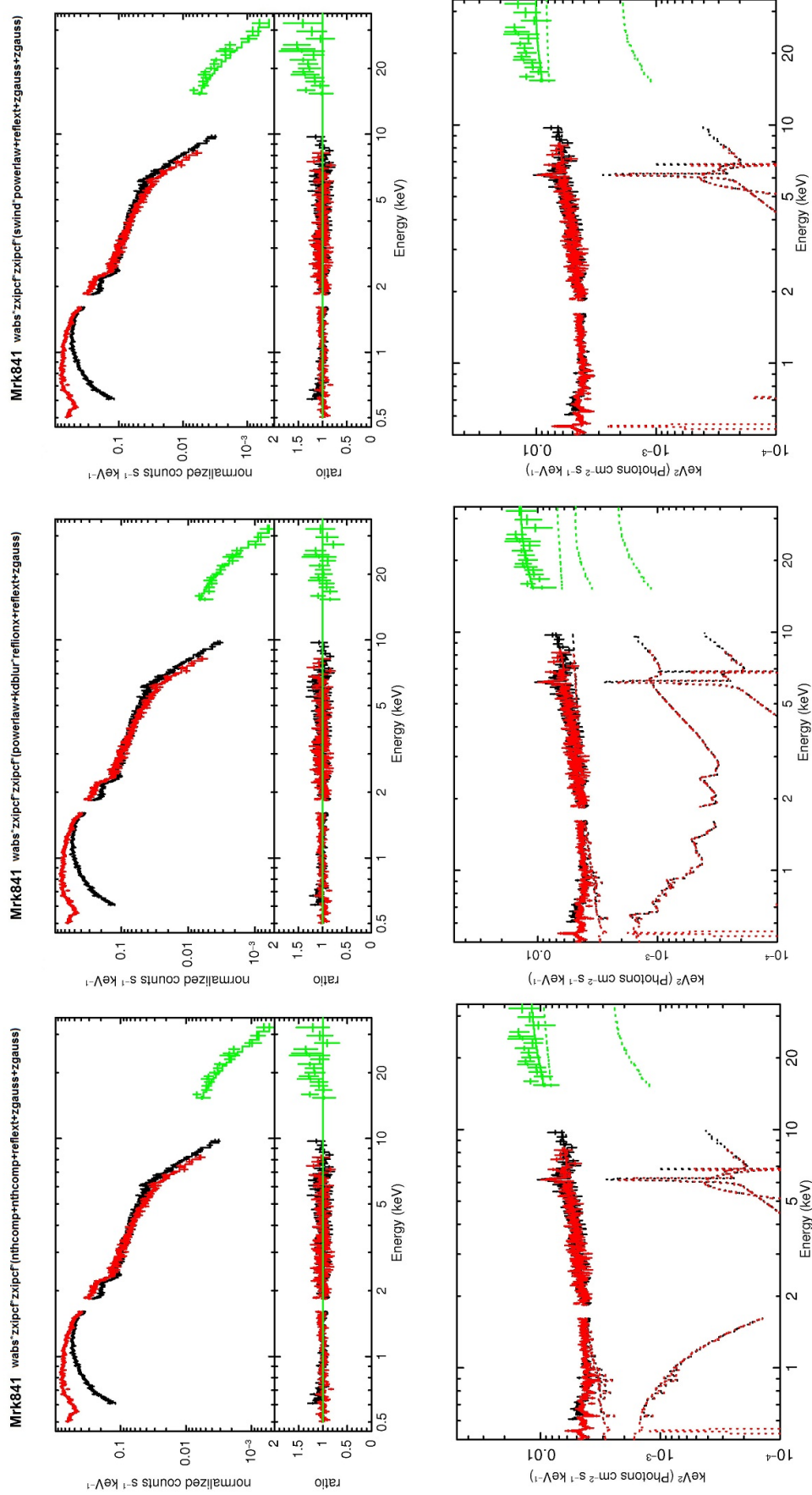


Figure 8. Top: Mrk 841 data (sum of *Suzaku* observations) and, in the subplot, data-to-model ratio. Bottom: unfolded data. Colour code for the different *Suzaku* instruments: *XIS/FI*-black, *XIS/I*-red and *HXD/PIN*-green. Three different models are shown, from left to right: double Comptonisation, blurred reflection and smeared absorption. Solid lines correspond to the best fit model, and thin dashed lines to the model different components. A broad emission line component is added for the double Comptonisation and the smeared absorption model only. The energy on the abscissa is in the observer frame. The data have been rebinned for clarity purposes.